minerals

MDPI

Article

Microbe-Mediated Mn Oxidation—A Proposed Model of Mineral Formation

Susanne Sjöberg [1,*], Changxun Yu [2], Courtney W. Stairs [3], Bert Allard [4], Rolf Hallberg [1], Sara Henriksson [5], Mats Åström [2] and Christophe Dupraz [1]

[1] Department of Geological Sciences, Stockholm University, SE-106 91 Stockholm, Sweden; rolf.hallberg@geo.su.se (R.H.); christophe.dupraz@geo.su.se (C.D.)
[2] Department of Biology and Environmental Sciences, Linneaus University, SE-39231 Kalmar, Sweden; changxun.yu@lnu.se (C.Y.); mats.astrom@lnu.se (M.Å.)
[3] Microbiology Group, Department of Biology, Lund University, 223 62 Lund, Sweden; courtney.stairs@biol.lu.se
[4] Man-Technology-Environment Research Centre (MTM), Örebro University, SE-701 82 Örebro, Sweden; bert.allard@oru.se
[5] Umeå Centre for Electron Microscopy (UCEM), Umeå University, SE-901 87 Umeå, Sweden; sara.henriksson@umu.se
* Correspondence: susanne.sjoberg@geo.su.se; Tel.:+46-(76)-27-69-001

Abstract: Manganese oxides occur in a wide range of environmental settings either as coatings on rocks, sediment, and soil particles, or as discrete grains. Although the production of biologically mediated Mn oxides is well established, relatively little is known about microbial-specific strategies for utilizing Mn in the environment and how these affect the morphology, structure, and chemistry of associated mineralizations. Defining such strategies and characterizing the associated mineral properties would contribute to a better understanding of their impact on the local environment and possibly facilitate evaluation of biogenicity in recent and past Mn accumulations. Here, we supplement field data from a Mn rock wall deposit in the Ytterby mine, Sweden, with data retrieved from culturing Mn oxidizers isolated from this site. Microscopic and spectroscopic techniques are used to characterize field site products and Mn precipitates generated by four isolated bacteria (*Hydrogenophaga* sp., *Pedobacter* sp., *Rhizobium* sp., and *Nevskia* sp.) and one fungal-bacterial co-culture (*Cladosporium* sp.—*Hydrogenophaga* sp. *Rhizobium* sp.—*Nevskia* sp.). Two of the isolates (*Pedobacter* sp. and *Nevskia* sp.) are previously unknown Mn oxidizers. At the field site, the onset of Mn oxide mineralization typically occurs in areas associated with globular wad-like particles and microbial traces. The particles serve as building blocks in the majority of the microstructures, either forming the base for further growth into laminated dendrites-botryoids or added as components to an existing structure. The most common nanoscale structures are networks of Mn oxide sheets structurally related to birnessite. The sheets are typically constructed of very few layers and elongated along the octahedral chains. In places, the sheets bend and curl under to give a scroll-like appearance. Culturing experiments show that growth conditions (biofilm or planktonic) affect the ability to oxidize Mn and that taxonomic affiliation influences crystallite size, structure, and average oxidation state as well as the onset location of Mn precipitation.

Keywords: *Hydrogenophaga*; *Pedobacter*; *Nevskia*; *Rhizobium*; *Cladosporium;* Ytterby mine; Mn oxidizers; Mn mineralization; biofilm; birnessite

Citation: Sjöberg, S.; Yu, C.; Stairs, C.W.; Allard, B.; Hallberg, R.; Henriksson, S.; Åström, M.; Dupraz, C. Microbe-Mediated Mn Oxidation—A Proposed Model of Mineral Formation. *Minerals* **2021**, *11*, 1146. https://doi.org/10.3390/min11101146

Academic Editors: Anna Panyushkina and Maxim Muravyov

Received: 6 September 2021
Accepted: 11 October 2021
Published: 18 October 2021

1. Introduction

Manganese biogeochemical cycling strongly affects groundwater, soil, and sediment composition in ecosystems through complex physicochemical and physiological pathways. Microbial communities have a seminal catalytic role in Mn oxidation [1], which is known to be kinetically very slow when carried out abiotically at Earth surface conditions

[2,3]. The resulting biogenic minerals are typically nanoparticulate birnessite-type Mn oxides [4], characterized by higher sorption capacity than abiotic/synthetic analogs [5]. These highly reactive minerals can thus efficiently accumulate and limit the mobility of metal ions in nature.

Precipitation of minerals containing oxidized Mn at the surface of the Earth typically involves closely connected biotic and abiotic processes, strongly dependent on local environmental conditions [6,7]. Although the production of biologically mediated Mn oxides is well established, relatively little is known about their morphological, structural, and chemical variations. Knowledge is also scarce when it comes to microbial-specific strategies for utilizing Mn in the environment and how these strategies contribute to and affect mineral formation and deposition. Defining such strategies and characterizing the associated mineral properties would contribute to a better understanding of their impact on the local environment and possibly facilitate evaluation of biogenicity in recent and past Mn accumulations.

Accumulations of Mn oxides were observed in a tunnel leading to the main shaft of the Ytterby mine, Sweden, in 2012. The precipitates occur as rock wall coatings associated with water-bearing fractures that emerge into a fully oxidized tunnel environment. In a recent study, the microbiomes in this ecosystem and their impact on metal mobility, were defined [8]. The study found that the fracture water was substantially depleted in Mn and other trace elements as it passes through the Mn precipitation zone down the approximately 2 m tall rock wall, and that a specific assemblage of bacteria are driving Mn oxidation and precipitation, thus indicating that these microbial groups have critical control on the end product (i.e., Mn oxides). This active, microbe-mediated deposit offers a unique opportunity to study Mn oxide formation and growth.

However, precipitation of Mn oxides from aqueous solutions often advances through a range of structurally diverse metastable phases incorporating Mn of various oxidation states [7,9]. As a result, Mn deposits such as those at the present field site, are typically mixtures of several different Mn minerals, which occur at different stages of mineralization, properties that make it problematic to identify and study early mineral growth stages catalyzed by microbes. In order to increase knowledge within this field, this work intends to supplement field data with data retrieved from culturing Mn oxidizers isolated from the field site, under controlled laboratory conditions. The objective of the work is to define depositional and structural varieties of biogenic Mn oxides generated from the culture experiments and compare these phases with the field site Mn oxides.

2. Study Site

The Ytterby mine is located on Resarö, an island about 30 km NE of Stockholm, Sweden (Figure 1). The studied Mn precipitates occur in a tunnel leading to the main shaft of the former quartz and feldspar mine located within a pegmatite body. The mine is also known for the discovery of Ta and seven of the rare earth elements (REE) [10,11]. The mine closed down in 1933, but reopened in the 1950s. This was the Cold War era and the Ytterby mine, just like many other mines in Sweden, was used as a fuel deposit for the Swedish Armed Forces. The approximately 400 m long tunnel system was constructed to link the old mine shaft with a quay used for loading and unloading the stored fuels. The tunnel is located at a shallow depth, 5 m above Baltic Sea mean sea level and 29 m below ground surface and goes through granitic and mafic rocks of varying chemical composition and metamorphic grade (see [12,13] for more details on the geological setting). In 1995, the storage of petroleum products was brought to an end and the mine shaft was emptied and closed down. The Mn oxides occur as rock wall coatings in a tunnel stretch located in the unsaturated zone ca 200 m away from the mine shaft where water bearing rock fractures emerge into the fully oxidized tunnel environment, which holds a nearly constant temperature of 8 °C year around. The vast majority of observed water bearing fractures are associated with Mn precipitates overlying a lithified layer of $CaCO_3$, while only a few are associated with moonmilk deposits, a soft, not lithified rock wall coating of

$CaCO_3$ [14]. The main components of the bulk precipitate are Mn (500 g/kg), Ca (65 g/kg), and REE (10 g/kg), and the predominant mineral is a microbe-mediated birnessite-type Mn oxide [8,15]. Powder X-ray diffractometry indicates that other poorly crystalline Mn phases are also present [15]. Despite the well-documented mineralogy of the Ytterby pegmatite, there are no other Mn minerals reported from the area, but there are a number of minerals in which Mn likely constitutes a minor component.

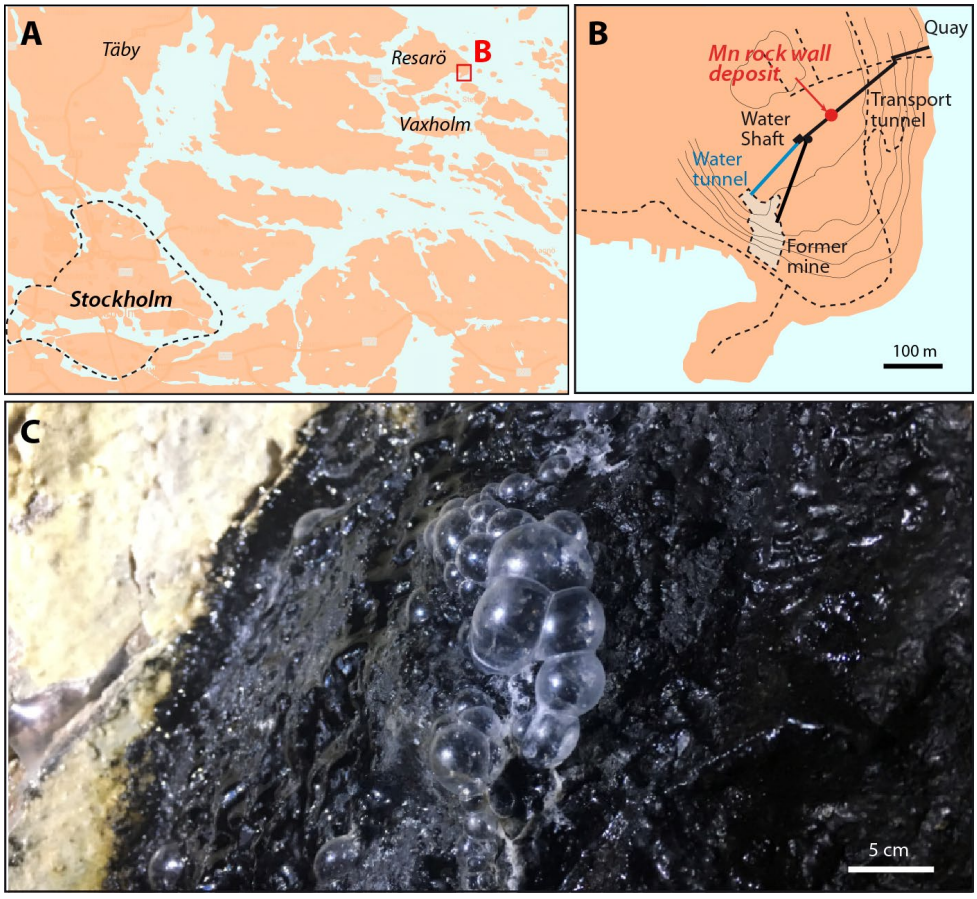

Figure 1. Maps showing the location of the Ytterby mine and the Mn deposit. (**A**) Map of the Stockholm area with position of Resarö and the Ytterby mine indicated. (**B**) Map of tunnel connecting the Ytterby mine shaft with a more recently constructed quay to the NE. (**C**) The Mn oxides precipitate from water provided by rock fractures that crop out in the tunnel. Modified from Swedish Fortifications Agency [16].

3. Materials and Methods

3.1. Isolation and Identification of Mn-Oxidizing Species

Bacterial and fungal strains were isolated from the Mn rock wall deposit in the Ytterby mine tunnel. Samples were collected from randomly chosen spots located in the area between the top and bottom of the rock wall. Sterile polypropylene spatulas were used to scrape off the Mn oxide precipitate from the tunnel wall, and the wet samples were collected directly in 100 mL Duran borosilicate bottles, containing a selective medium for enrichment and isolation of Mn-oxidizing microorganisms. The medium is composed of sodium bicarbonate and monopotassium phosphate-buffered basal mixture (50 mgL^{-1} $Ca(NO_3)_2{\cdot}4H_2O$; 10 mgL^{-1} $CaCl_2{\cdot}2H_2O$; 50 mgL^{-1} $MgSO_4{\cdot}7H_2O$; 10 mgL^{-1} KH_2PO_4; 5 mgL^{-1} $Na_2SiO_3{\cdot}9H_2O$; 10 mgL^{-1} $NaHCO_3$), nutrients (1.5 gL^{-1} yeast extract and 5 gL^{-1} tryptone for enrichment and 0.5 gL^{-1} yeast extract and 2.5 gL^{-1} tryptone for isolation), and manganese mixtures (5 gL^{-1} $MnSO_4{\cdot}4H_2O$ for enrichment and 3 gL^{-1} $MnSO_4{\cdot}4H_2O$ for isolation). The nutrients and Mn mixtures were prepared separately and sterile-filtered (0.2 µm), then added into the cooled autoclaved basal mixture with a final pH of 6.8. After inoculation,

the bottles containing liquid cultures were covered with aluminum foil and placed at 8 °C to mimic in situ environmental conditions. After four weeks, cultures were transferred onto low nutrient agar plates, Reasoner's 2A, from Merck Millipore (Darmstadt, Germany) streaked by the Mn containing enrichment and/or isolation media as described above. The inoculated plates were wrapped in aluminum foil and thereafter placed at 8 °C in an oxic environment. Microscopy analyses were conducted on portions of cultures grown on solid media, collected and analyzed when the first Mn precipitates were spotted (Leica stereo microscope, Leica Microsystems, Wetzlar, Germany) and then once a month during six months. Uninoculated plates were monitored for any abiotic Mn precipitation.

Qualitative Mn oxidation was assessed with leucoberbelin blue (LBB) staining as described by Krumbein and Altmann (1973) [17] and Tebo et al., (2007) [18]. A drop of LBB solution was added to a colony surface. A blue staining on or in the vicinity of the colony confirmed the presence of oxidized Mn. Liquid cultures were filtered using Whatman grade GF/F borosilicate glass microfiber filters (Cytiva, Maidstone, United Kingdom) and the LBB solution was then added to the filters.

Colonies associated with Mn oxidation were repeatedly transferred to new plates until pure cultures or cultures dominated by a few Mn-oxidizing species were obtained and thereafter identified using a two-step polymerase chain reactions (PCR) protocol with the universal primers' combination: 519 forward and 1391 reverse as described in Spang et al. (2015) [19], using HotStarTaq (Qiagen, Hilden, Germany). Microbial colonies diluted in sterile PCR grade ddH_2O (HyClone, Logan, United States) and gently vortexed, were used as templates for PCR without prior DNA extraction. Amplification of the targeted small subunit rRNA gene was conducted on 1 uL diluted microbial colony suspension. Samples were sequenced on a MiSeq Illumina platform using Reagent kit v3, (600-cycle) at the SciLifeLab sequencing facility at Uppsala University, Sweden. Reads were processed using QIIME2 pipeline [20]. Briefly, forward reads were denoised using dada2 and clustered into sequence features using vectorized search (VSEARCH). Taxonomy was assigned using a naïve Bayesian classifier in QIIME2 (feature-classifier classify-sklearn) using a confidence score of 0.7 (--p-confidence) against the SILVA v138 database [21,22]. The QIIME2 workflow used in this study is given as Supplementary Material (S1). Sequences were also compared using the National Center for Biotechnology Information (NCBI) blast network service. Sequences were deposited in the NCBI Sequence Read Archive (SRA) under Sequence Read Run (SRR) accession numbers SRR9202442, SRR9202456, SRR9202435, and SRR9202458 (NCBI Sequence Read Archive, 2021) [23] (S2).

3.2. Characterization of Mn Minerals in Cultures and the Field Site Samples

3.2.1. Environmental Scanning Electron Microscopy

Microbial cultures as well as field site samples were screened for Mn oxide mineralizations with a Quanta environmental scanning electron microscope (ESEM, Thermo Fisher Scientific, Waltham, MA, USA) equipped with a field emission gun (FEG 650). The field site samples were kept in conditions similar to those in the tunnel environment (cold and dark) during transportation. The samples were then air-dried in a desiccator and put on stubs covered by carbon tape. Colonies were scraped off the agar plates and put on stubs covered by carbon tape. Two different detectors were used during the SEM analyses: a large-field detector (LFD) and a circular backscatter detector (CBS). An energy dispersive X-ray spectrometer (EDS) was used for compositional information. Selected samples were further imaged and analyzed using a JEOL JSM-7000F equipped with EDS with resolution 137 eV at the Department of Materials and Environmental Chemistry, Stockholm University, Sweden. For Figure 5B–E, samples were fixed in 2.5% glutaraldehyde (TAAB) in 0.1 M Sodium cacodylate buffer, dehydrated in a series of graded ethanol, and critical point dried (Leica EM300CPD). Images were acquired using the BSE detector with EVO SEM (Zeiss). For Figure 5F, samples were in addition coated with 5 nm chromium and acquired using the in-lens SE detector with Merlin FESEM (Zeiss, Oberkochen, Germany).

Samples were also frozen in nitrogen slush, cold-fractured, freeze-etched, and coated within a preparation chamber (Gatan, Alto 2500, Gatan, Inc. Pleasanton, CA, USA) for low temperature imaging, using methodology described in Dupraz et al. (2013) [24].

3.2.2. Transmission Electron Microscopy

Bacterial specimens were scraped off the cultivated agar plates, put in LB medium and thereafter high pressure frozen in an HP100 (Leica microsystems). Frozen samples were freeze substituted in a Leica EM AFS2 using the processing robot (Leica, Wetzlar, Germany) according to the protocol by Hawes et al. (2007) [25] and finally embedded in HM20 (polysciences). Ultrathin (70 nm) sections were obtained using a diamond knife. Owing to the brittleness of the Mn oxides, many of the larger crystals fell off during sectioning, leaving behind imprints in which only small patches of the original precipitates were preserved. A selection of sections were post-contrasted with 5% uranyl acetate and Reynolds lead citrate [26], while the remaining ones were left untreated for accurate elemental energy dispersive X-ray analysis. For the field site samples, a few milligrams of ground Mn precipitates were dispersed in deionized water. The dispersed solution was dropped onto a carbon film supported Cu grid and air-dried. Sections and field site precipitates were used for imaging, microstructural analysis based on selected area electron diffraction patterns (SAED), and high-resolution transmission electron microscopy (HRTEM). Samples were examined with a Talos 120 C (FEI, Eindhoven, The Netherlands) operating at 120 kV. Micrographs were acquired with a Ceta 16 M CCD camera, using TEM Image & Analysis software v. 4.17. In addition, HRTEM and SAED patterns were obtained on a JEOL JEM 2100 F operating at 200 kV equipped with an EDS (resolution 138 eV) and a JEOL JEM 2100 operating at 80 kV at the Department of Materials and Environmental Chemistry, Stockholm University.

3.2.3. X-ray Absorption Spectroscopy

Manganese K-edge X-ray absorption Near Edge Structure (XANES) spectra were collected in transmission mode at the Balder beamline at the MAX-IV laboratory (Lund, Sweden). The storage ring was operated at 3.0 GeV and ~250 mA. The incident X-ray beam, tuned by a pair of Si (111) crystals, had a transmitted flux of 10^{-12}–10^{-13} photons/s [27]. Prior to measurements, the X-ray beam was focalized into a 150 μm (v) × 350 μm (h) spot and the energy of the X-ray beam was calibrated by assigning the first inflection point of a Mn foil at 6539 eV. Before being mounted between two layers of Kapton tape, the wet specimens of field site Mn precipitates were homogenized with an agate mortar, while cultures grown for approximately 3 months on agar substrates were cut into small pieces. The mounted agar substrates were scanned vertically or horizontally in order to locate biofilms (as indicated by strong Mn absorption) for subsequent XANES measurement. The XANES spectra of the sample specimens were collected at room temperature from approximately −160 to +200 eV relative to the Mn K-edge using a fly scan mode. XANES spectra were also collected for selected Mn oxide references (manganosite, hausmannite, bixbyite, pyrolusite and Mn(II)-sorbed humic acid). The Mn oxide references were purchased from Sigma-Aldrich, while the Mn(II)-sorbed humic acid was prepared according to Yu et al. (2016) [28]. The spectra of the Mn oxide references (diluted with polyethylene to achieve ideal Mn concentrations) and the Mn(II)-sorbed humic acid were recorded using the same setup as the sample specimens. To get satisfactory signal to noise ratios, 4–7 scans of each reference and 5–11 scans of each sample specimen were recorded. Reproducibility of the multiple scans confirms no radiation-induced damage during the measurement. The scans for each sample and reference were aligned, merged, background-subtracted, and normalized using the Athena program [29].

To further assist the interpretation of the sample spectra, the spectra of three Mn(III) hydroxides (groutite, feitknechtite, and manganite), a tunnel-structured Mn oxide (todorokite) and rhodochrosite, and two hydrous layered phyllomanganates (hexagonal

birnessite and triclinic birnessite), collected by Bargar et al. (2005) [6], Feng et al. (2010) [30], and Yu et al. (2017) [31], respectively, were also included.

4. Results and Discussion

4.1. Isolated Mn-Oxidizing Microorganisms

Cultures yielded four bacterial strains (*Hydrogenophaga* sp., *Pedobacter* sp., *Rhizobium* sp., and *Nevskia* sp.) and one fungal-bacterial co-culture (*Cladosporium* sp.—*Hydrogenophaga* sp.—*Rhizobium* sp.—*Nevskia* sp.) with varied abilities to deposit minerals containing oxidized Mn. Members of the *Pedobacter* and *Nevskia* genera were previously not known to oxidize Mn while the three other taxa were known to. Members of the *Nevskia* genus were previously shown to be highly abundant at the field site, while the relative abundance of the other strains only accounted for a maximum of 0.09% [8,32]. *Hydrogenophaga* spp. have been identified as important members of microbial communities associated with Mn oxidation in drinking water systems [33], and biofilters [34], while species belonging to the *Rhizobium* genus have been associated with Mn oxidation in subsurface deposits [35]. Fungi that belong to the *Cladosporium* genus have been associated with Mn oxidation in metal-rich mine environments [35,36] and with sequestration of Mn inside hyphal cells [37]. We were able to obtain pure cultures of the *Hydrogenophaga* sp. as well as the *Pedobacter* sp. while the *Rhizobium* sp. and *Nevskia* sp. were only observed growing together. Results from this study did thus not allow us to determine whether *Rhizobium* sp. and *Nevskia* sp. were capable of Mn oxidation on their own or if they have developed a synergistic relationship. As for the *Cladosporium* sp. co-cultures, the bacterial species were not detected in microscopy images, but were present in the rRNA gene sequence analysis. We assume that these cultures were dominated by *Cladosporium* sp., but that the bacterial consortia was present in varying proportions. *Pedobacter* sp. only precipitated Mn oxide on solid substrate, whereas *Hydrogenophaga* sp. was observed to produce Mn oxide both on solid and in liquid media. Scanning electron microscopy (SEM) coupled to electron dispersive spectroscopy (EDS) showed that the majority of Mn oxides produced by the cultured bacteria also contained small amounts of P originating from the growth medium. No Mn oxides were detected in the negative controls containing the Mn(II) medium, except without inoculated bacteria.

4.2. Products of Mn(II) Oxidation in Cultures

4.2.1. *Hydrogenophaga* sp.

Hydrogenophaga sp. produced punctiform to small circular-shaped gelatinous colonies with slightly undulated margins. Mn oxide precipitates accumulated in a well-constrained area in the center of the carotenoid pigmented colonies, giving them a fried-egg appearance (Figure 2). Circular-shaped aggregates of Mn oxide particles were produced. These aggregations had a core of rod-shaped crystals that were of similar size and shape as bacterial cells (Figure 2C–E). TEM images indicated that nucleation begun in close association with bacteria. The precipitates were observed (1) within the bacteria that ended up filled with Mn oxide within a well-preserved cell wall (Figure 2G) or replacing the cell wall (Figure 2H), as well as (2) filling the space in between bacteria with branching blade-like precipitates (Figure 2G, arrows). In the case of infillings, Mn mineralization rapidly overtook the cells leading to death. There were no signs of early precipitates on the wall of healthy cells. The remains of mineralized bacterial cells were bound together by networks of branching blade-like precipitates that ultimately built the micrometer spherical aggregates of Mn oxides observed in Figure 2A–D,F.

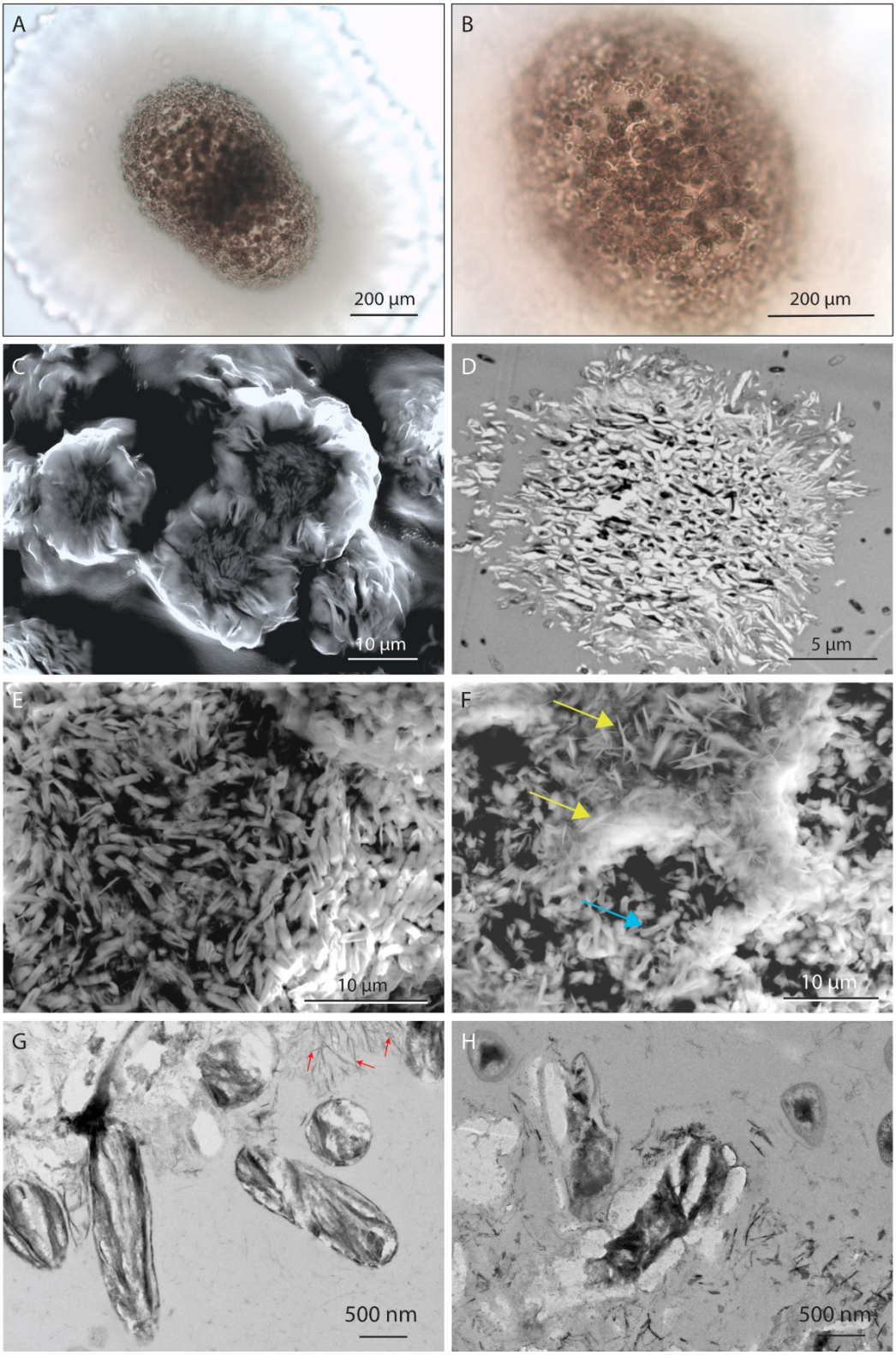

Figure 2. Micrographs of an isolated Mn(II) oxidizing bacterium, *Hydrogenophaga* sp., and associated Mn precipitates. (**A**,**B**) Light-microscopy images showing a colony with Mn precipitates located at the center, giving them a fried-egg appearance. (**C**) SEM image showing close-up of Mn precipitates in (**A**,**B**). (**D**) TEM image showing bacteria trapped in an aggregate of Mn oxide particles. (**E**) SEM image showing rod-like crystals of similar size and shape as the bacterial cells. (**F**) Growth of blade-shaped crystals (yellow arrows) forming a matrix that bind together the remains of mineralized bacterial cells (blue arrow). (**G**) TEM image of mineralized bacteria with preserved cell walls. Red arrows also showing Mn precipitates filling the space in between bacteria with branching blade-like precipitates. (**H**) Mineralized bacteria embedded in sheaths of Mn precipitates.

Mn precipitates mainly occurred as: (1) nanoscale wavy sheets and (2) more blade-shaped crystals (S3). The SAED pattern associated with the wavy sheets had diffuse diffraction rings, and weak reflections at ~7.2 and ~3.6 Å that fit well with the (001) and (002) basal planes in birnessite (S3A). There were also weak reflections at ~2.1, ~1.7, and ~1.4 Å, but the characteristic ~2.4 Å (100) reflection in birnessite from previous studies [38–40] was absent. Instead, there were comparatively strong reflections at 3.0 and 2.6 Å. The sturdier, blady crystals produced a polycrystalline SAED pattern with reflections at ~8.5, 6.0, 4.8, 4.1, 3.5, 3.0, 2.6, 2.2, 2.1, 1.7, 1.5, and 1.4 Å of randomly oriented crystallites (S3B). Overall, the reflection points corresponded reasonably well with todorokite (amcsd 0001189).

The timing of precipitation of the observed crystal shapes/phases cannot be clearly determined based on these data. Todorokite has however been documented to form from birnessite precursors [41,42]. It is therefore possible that the initial wavy sheets (birnessite-like) progressively transform into more blady crystals (todorokite) with time. The same 3.0 and 2.6 Å reflections observed in the wavy sheet precipitates were also observed in the more blade-shaped precipitates, indicating a possible transition between the two phases. However, the d-spacing along the [100] direction (reflecting the tunnel width for todorokite) was only ~8.5 Å, which differ from a typical width of 9.6 Å. Varying tunnel widths (ranging from 6 to 16 Å) are not uncommon in todorokite formed from birnessite precursors [41,42].

The way *Hydrogenophaga* sp. induces precipitation of Mn oxides is still elusive as the ecological strategy of forming compact and dense colonies in the presence of Mn is puzzling. This behavior could result from intense metabolic activities, indirectly leading to Mn oxidation, in a tightly packed community. It is also possible that the rapid cell division itself is a stress escape strategy to resist death by mineralization. Whatever the processes responsible for Mn oxidation, close interaction between precipitates and cells is observed. Mn oxidation within the cell causes rapid mineralization of the inner part, causing the bacterium to die. Mineralization linked to the replacement of the cell wall and precipitation in between the mineralized cells is more difficult to interpret. The fact that deposition of Mn oxides seems to take place after the cells died indicates that a non-physiological mechanism is at work. Previous studies have argued that cation adsorption to bacteria could be enhanced after the death of the organisms possibly due to enhanced exposure to binding sites [43,44]. However, catalysis of Mn(II) oxidation by already formed Mn oxides, i.e., autocatalytical oxidation, is not expected to occur at pH below 9 [1,6], and thus not likely in the present growth medium buffered at circumneutral pH. It is also possible that *Hydrogenophaga* sp. flagella serve as templates for the deposition for the branching precipitates. Comparable deposition of branching Mn particles, embedding and connecting cells, were previously observed in cultures of *Pedomicrobium*-like bacteria [45]. In this case, Mn particles were deposited on fine extracellular polymer filaments. The precipitation was inhibited but not completely stopped when treated with glutaraldehyde or heat, which suggested that an unusually stable enzyme was involved in this process [45].

4.2.2. *Pedobacter* sp.

The *Pedobacter* strain produced large (up to 1 cm in diameter), circular, slightly domed mucoid colonies with smooth margins. As the colonies matured, they merged and formed large amounts of slimy mucilaginous mass in which abundant circular Mn oxides formed (Figure 3), possibly in association with double layer membrane vesicles released from the cells. Spherical aggregates of Mn oxides were produced (*cf*. *Hydrogenophaga* sp.), but without the core of mineralized bacteria. Note that most of the Mn precipitates fell off during sectioning, leaving behind white imprints in which only small patches of the original precipitates are preserved. The early stages of Mn mineralization were observed in the mucilaginous extracellular secretions, at some distance from the cell. TEM images indicated that double membrane vesicles released by the cells acted as preferential nucleation sites for the Mn oxides (Figure 3F–H). No intracellular precipitation was observed.

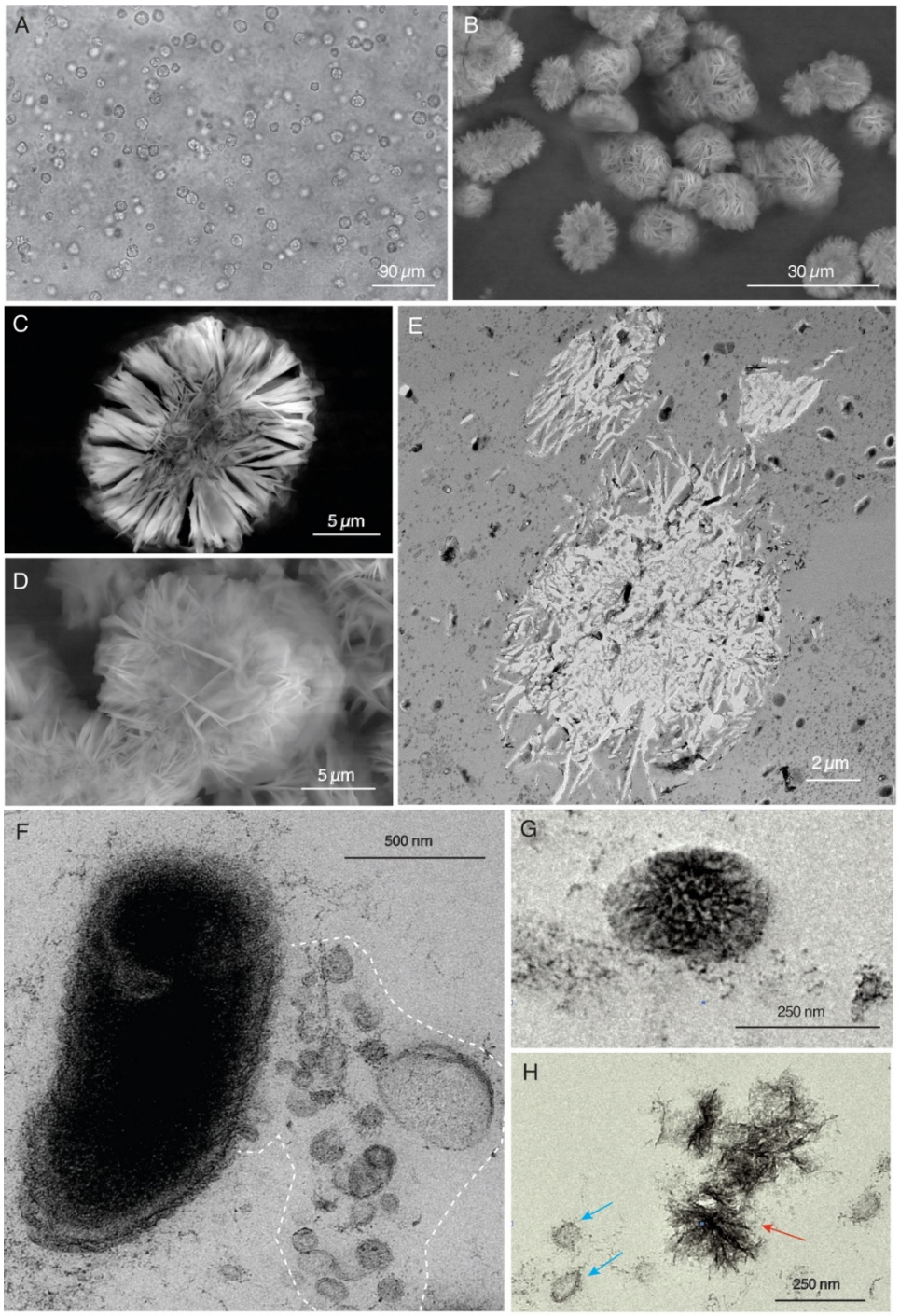

Figure 3. Micrographs of an isolated Mn(II) oxidizing bacterium, *Pedobacter* sp., and associated Mn precipitates. (**A**) Light-microscopy image showing numerous spherulites constructed of nano- to micro-meter sized sheets. (**B**) SEM image of (**A**). (**C**,**D**) SEM images of spherulites. (**E**) TEM image of Mn oxide aggregate. (**F**) TEM image of cell releasing vesicles of varying sizes from the outer cell membrane. (**G**) Mn oxides covering a possible vesicle. (**H**) Patches of Mn oxides forming in the mucilaginous colonies (red arrow) and double membrane vesicles (blue arrows).

Previous studies have demonstrated that most bacterial Mn oxidation and precipitation takes place extracellularly, and in the case of enzymes being involved, these are thought to be located at the outer parts of the cell (outer membrane or sheath) [46–48], or as components of the outermost layer of spores [49–51]. A few studies have also reported on the association of Mn precipitates with vesicles, similar to the observations in this work. Larsen et al. (1999) [44] showed that Mn-oxidizing activity was localized in double-

layered membrane vesicles in the outer membrane of a *Pedomicrobium* species. Oxidized Mn was also found in minerals precipitating around extracellular vesicles through anaerobic Mn oxidation by cultures of anoxygenic phototrophs [52]. Ehrlich and Salerno (1990) [53] additionally suggested that bacterial membrane vesicles coupled ATP synthesis (energy conservation) to Mn(II) oxidation.

4.2.3. *Nevskia* sp.—*Rhizobium* sp.

Oxidized Mn was mainly found in minerals that were deposited on *Nevskia* sp. cell walls and associated organic material, possibly their acellular stalks. The mixed cultures produced slightly raised long colony strings with a dark hazy center and entire to undulating margins in which pinkish Mn precipitates were located (Figure 4). In addition to Mn and O, these areas also contained varying amounts of P and Na, either adsorbed on the organic matter or part of the mineral structure. In contrast to the diffuse diffraction rings and polycrystalline SAED pattern observed in *Hydrogenophaga* sp. colonies, the obtained SAED pattern for the analyzed precipitate associated with organic matter in *Nevskia-Rhizobium* spp. likely reflected one crystal (Figure 4G). Except for 7.2 Å reflections which suggested the presence of a 7 Å phyllomanganate, the mineral also had a ~13 Å periodicity, indicative of a large unit cell (Figure 4G). Mn mineralization was not observed in samples in which no stalk-like organic matter was in close contact with the cells. Instead, *Nevskia* sp. cells developed thick sheaths and typically had 2–5 intracellular globules that were less electron dense compared to the rest of the cell (Figure 4C). Similar inclusions in *Nevskia* sp. cells have previously been interpreted to be gas vacuoles and/or carbon storage polymers, commonly referred to as polyhydroxyalkanoates [54,55]. The *Rhizobium* cells were frequently observed having electron dense angular particles inside the cells (Figure 4E,F). A certain amount of these inclusions did not diffract and were mainly composed of C, O, N, and Na. Some other inclusions diffracted, and showed, in addition to the above elements, the presence of small amounts of Mn, P, and Cl.

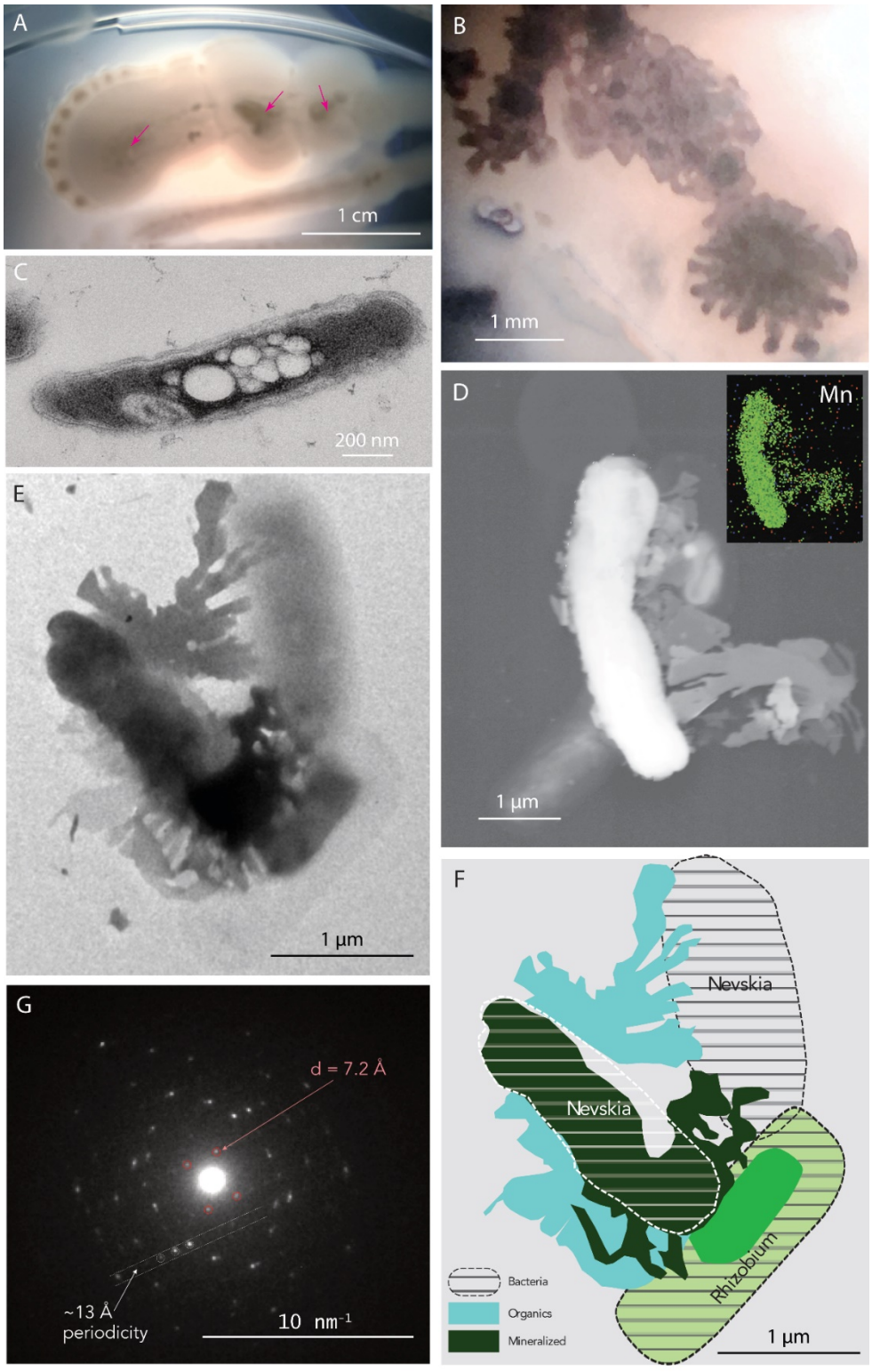

Figure 4. Micrographs of *Nevskia-Rhizobium* spp. and associated Mn mineralizations. (**A**) Mixed *Nevskia-Rhizobium* spp. colony grown on agar substrate with cluster of Mn precipitates in the center of the colonies (pink arrows). (**B**) Close-up of Mn precipitates. (**C**) Sheathed *Nevskia* sp. cell with intracellular globules (less electron dense), which possibly are gas vacuoles and/or carbon storage polymers. (**D**) SEM image of mineralized *Nevskia* sp. cell and associated organic matter (possibly their acellular stalks). (**E**,**F**) TEM image showing cluster of bacteria and organic matter and associated mineralizations. To the left, a mineralized *Nevskia* sp. cell and associated organic matter (possibly

their acellular stalks). At the bottom right, a *Rhizobium* sp. bacterium containing electron dense angular particles inside the cell. (**G**) SAED of mineralized *Nevskia* sp. cell and associated organic matter in (**E**).

It was not possible to isolate *Nevskia* sp. or *Rhizobium* sp. separately in this study, and it cannot be assessed whether these strains developed a synergetic relationship to oxidize Mn or whether they can do it separately. No, or very little Mn precipitation was however associated with *Rhizobium* sp. cells. *Nevskia* spp., which are epineuston stalked bacteria (bacteria living at the water surface and producing thin extensions out of the cell wall), representing the most abundant genus in a micrometer thick gas-trapping biofilm located on the surface of the precipitated Mn oxides in Ytterby (see details in [8,32]). Its involvement in the Mn oxide producing ecosystem is not yet clear, but results from this study indicate that *Nevskia* spp. are capable of producing Mn oxides during certain stages of its lifecycle and under dark and cold conditions. Only one previous report [55] indicates precipitation of metals (Fe but no Mn) on the laterally excreted stalks of *Nevskia* spp.

Rhizobium sp. was also frequently found growing together with *Hydrogenophaga* sp. on plates. In these cases, the small round yellow *Hydrogenophaga* sp. colonies grew on top of or within the *Rhizobium* sp. colonies, forming long strings of Mn precipitates.

4.2.4. *Cladosporium* sp.—*Hydrogenophaga* sp.—*Rhizobium* sp.—*Nevskia* sp.

The retrieved Mn-oxidizing fungal-bacterial co-culture produced dark green to black colonies. The bacterial species (*Hydrogenophaga* sp.—*Rhizobium* sp.—*Nevskia* sp.) were not detected in microscopy images, but were present in the rRNA gene the sequence analysis. We assume that these cultures were dominated by *Cladosporium* sp., but that the bacterial consortia was present in varying proportions. Manganese precipitates were primarily deposited as globular particles that were spatially separated from the hyphae, but also as knot-like aggregates deposited on hyphal surfaces (Figure 5). The spatially separated Mn globules were distributed within the hyphal network. The microscale particles consisted of nanoscale plates that had an undulated, almost serrated, margin. EDS analysis showed that the particles were composed of Mn, O, and P.

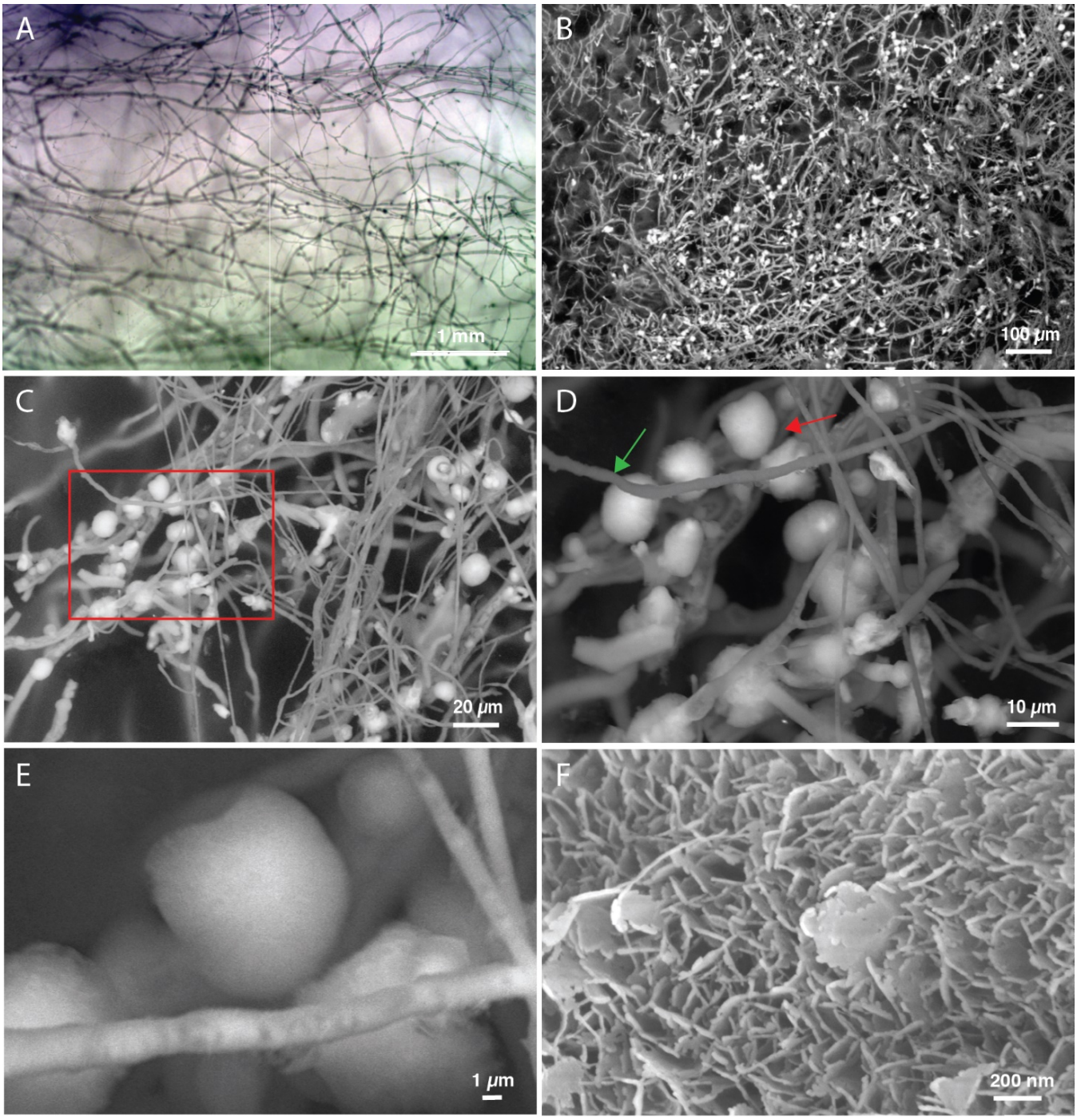

Figure 5. Micrographs of a Mn(II)-oxidizing fungal-bacterial co-culture containing a fungal species belonging to the *Cladosporium* genus within the Ascomycota phylum and a consortium of bacteria. (**A**) Light microscopy showing the complex network of hyphae. (**B**) SEM image of (**A**). (**C**) SEM images showing the association of hyphae and Mn oxide precipitates. (**D**) Mn precipitates (red arrow) are deposited as globular particles on hyphal surfaces (green arrow). (**E**) Close-up of (**D**). (**F**) SEM image of Mn oxide nanosheets having undulated, almost serrated, margins.

4.3. Products of Mn(II) Oxidation at the Field Site

4.3.1. Microscale

The bulk material sampled in the field consisted primarily of three Mn oxide microstructures: (1) dendrites (2) botryoides, and (3) wad-like globular particles (Figure 6). Both the dendrites and botryoides had a distinct growth direction and showed a morphological continuity from thin shrub-like dendrites to the globular massive botryoide end-member (Figure 6I–N). Individual dendrites-botryoides ranged from about 10 to 100 µm in length.

The wad-like globular Mn oxides occurred as solitary particles (typically 2–5 μm in diameter) or clusters, used as building blocks in the formation of the dendrites-botryoides. These particles, which grew radially around one nucleus or had a polycrystalline fibrous internal structure either formed the base for further growth into dendrites-botryoids or were fused onto an existing structure. EDS analyses indicated that the main cation, after Mn, in these structures was Ca. Cell-like structures and filaments of varying thickness and lengths were often associated with the Mn oxides, particularly in the initial growth areas. The relatively chaotic mix of organic traces and early Mn oxide particles became capped by denser, laminated precipitates, implying an iterative growth process. Light and dark alterations expressed variations in Mn and Ca concentrations, but also in the Mn:Ca atomic ratio. Mn and Ca concentrations were higher in the darker bands than in the lighter, while the higher reflectance areas had higher Mn:Ca ratios. Similar laminated structures are observed in other studies on Mn oxides, and it has been suggested that the rhythmic growth pattern reflects a gradual mineralization process over time as a response to Mn(II) concentrations in the surrounding water [35]. The vague radial texture around the nuclei of individual wad-like globules was no longer observed in globules that were fused onto a growing botryoid. Irrespective of morphology and growth pattern, all morphologies had a similar surface structure: nanometer thick sheets forming a reticulated texture (Figure 6C).

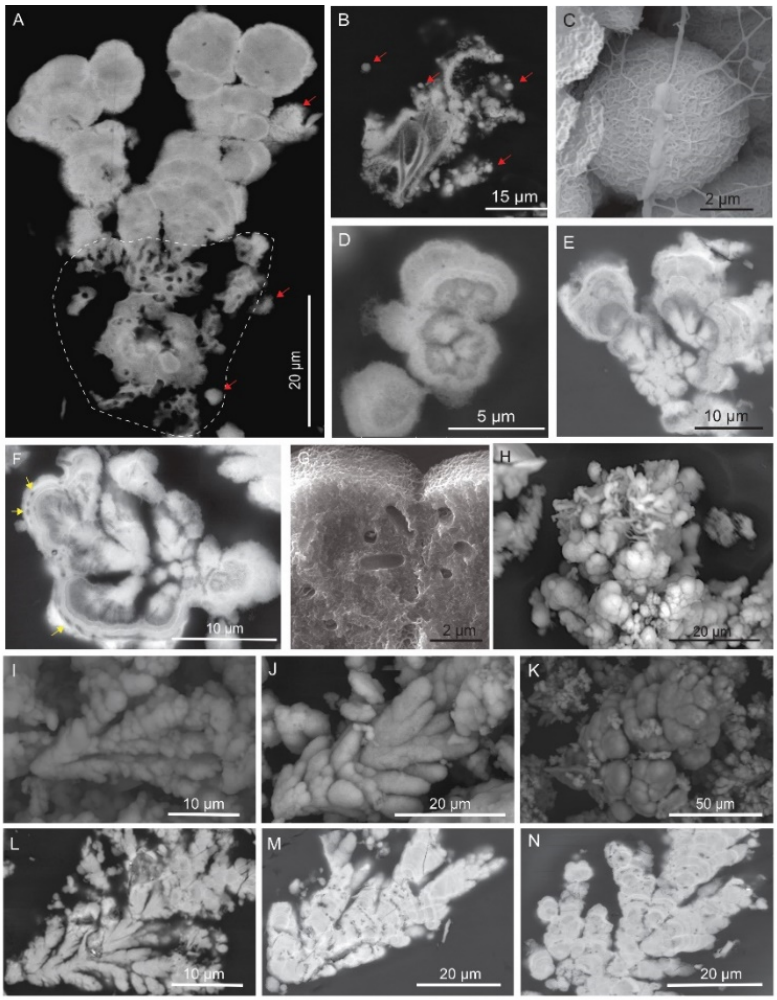

Figure 6. SEM images showing microstructures of the Ytterby rock wall Mn oxides. (**A**) Uncoated polished thin section showing laminated branches of dendritic-botryoidal Mn oxides growing on nucleation area (dashed). (**B**) Uncoated polished thin section of nucleation area showing Mn oxide encrustation of microbial remnants (filaments and cell-like structures) and wad-like Mn oxides occurring as solitary particles and in clusters (red arrows). (**C**) Cryo-SEM image showing nanometer

thick sheets forming a reticulated surface texture of Mn oxide particle. (**D**) Cross section of wad-like Mn oxide particle. (**E**,**F**) Initial growth area capped by laminated Mn oxide precipitates. Note the embedded cell like structures (yellow arrows). (**G**) Cryo-SEM image showing cell-like structures embedded in microsperolitic/botryoidal Mn oxide microstructures (**H**) Filaments of varying thickness covering Mn oxides. (**I**–**M**$_{I; J; K; L; M;}$) SEM images showing dendritic-botryoidal microstructures in the Ytterby Mn oxides. (**I**–**K**$_{I; J; K; I; J; K; L; M;}$) Morphological continuity from thin shrub-like dendrites to the globular massive botryoid endmember. (**L**–**N**$_{L; M; N; I; J; K; I; J; K; L; M;}$) Polished cross sections of (**I**–**K**$_{I; J; K; L; M; N; I; J; K; I; J; K; L; M;}$).

4.3.2. Nanoscale

High-resolution transmission electron microscopy (HRTEM) images and electron diffraction patterns were combined with EDS to study nanostructures in the field site Mn precipitate. The dendritic-botryoidal growth pattern observed at the microscale was no longer visible in the nanoscale analyses. Instead, three types of areas were identified, from here on referred to as type 1, 2, and 3 (Figure 7).

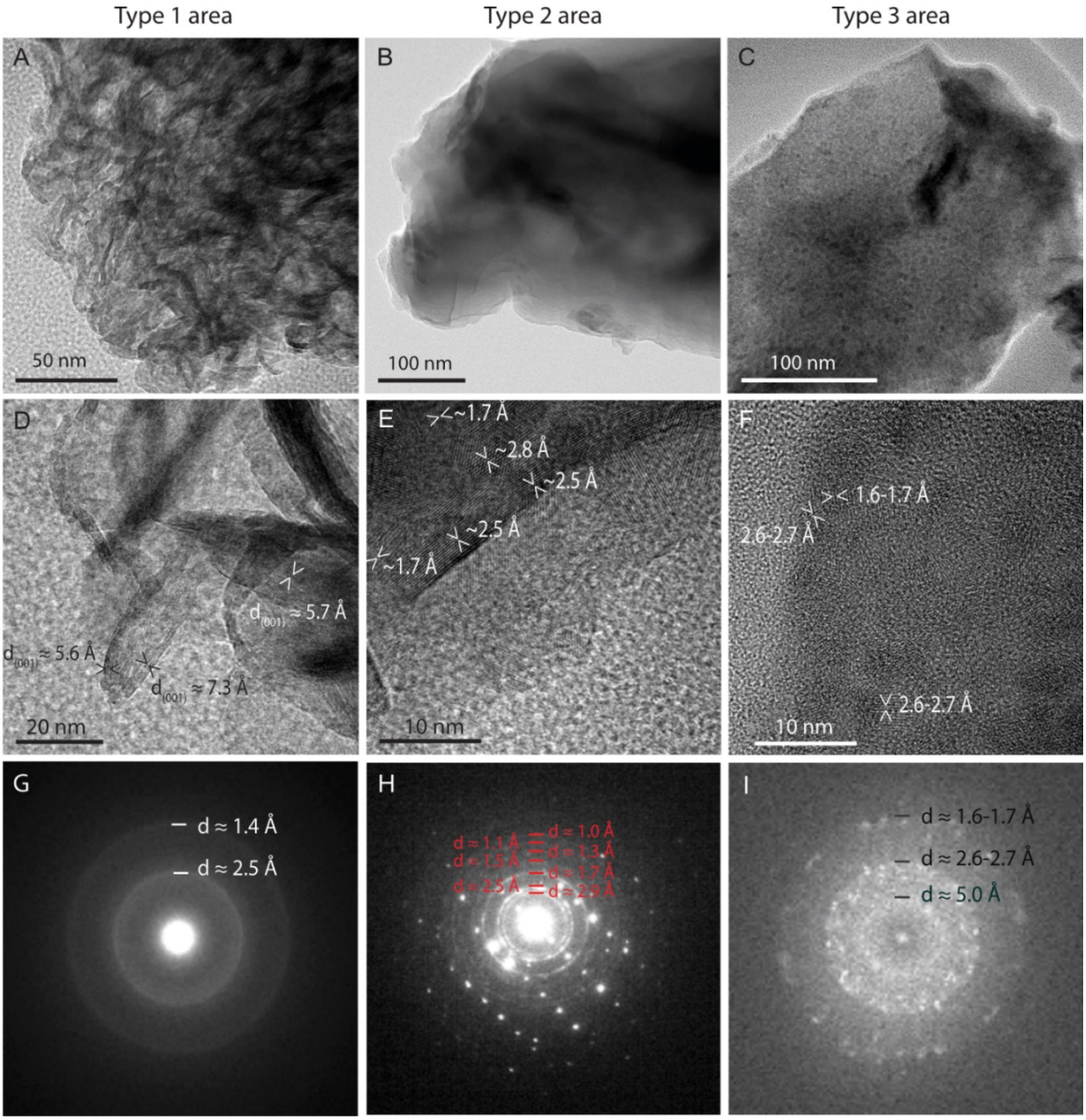

Figure 7. TEM images showing three nanoscale type areas in the field site Mn precipitates. (**A**) Sheets constructed of very few layers elongated along the octahedral chains. In places, the sheets bend and curl under to give a scroll-like appearance. (**B**) Polycrystalline sheets. (**C**) Flakes with particles. (**D**,**G**) HRTEM and SAED pattern of sheets in (**A**). (**E**,**H**) HRTEM and

SAED pattern of polycrystalline sheets in (**B**). (**F**,**I**) HRTEM and the corresponding fast Fourier Transform (FFT) pattern of particles in (**C**). (**G**) SAED of (**A**).

The most commonly observed nanoscale structure was the type 1 area, which was characterized by networks of Mn oxide sheets constructed of very few layers and elongated along the MnO_6 octahedral chain. (Figure 7A). HRTEM images showed a layered structure in which the distance between basal planes varied from 5.6 to 7.3 Å and lattice fringes with a 2.4–2.8 Å interlayer distance (Figure 7D). The corresponding selected area electron diffraction (SAED) pattern had two diffuse diffraction rings at ~2.5 and ~1.4 Å (Figure 7G). These data fit well with Mn oxides that are structurally related to birnessite, which is constructed by layers of edge-sharing MnO_6 octahedra with interplanar spacings typically around 7 Å [56,57]. A ~5.6 Å separation has been observed in dehydrated 7 Å phyllomanganates [58–60]. The absence of (001) and (002) basal plane reflections ($d_{(001)}$~7.2 Å, $d_{(002)}$~3.6 Å) in the SAED is a characteristic feature for layered Mn oxides that have very few and randomly oriented stacked sheets along the c-axis [39,40,61,62]. The sheets appeared to grow preferentially along the a or b axis and were typically a few hundred nm long. In places, the sheets bent and curled under to give a scroll-like appearance. Type 2 areas were characterized by denser nanoscale Mn oxide sheets compared to the type 1 area and produced a polycrystalline SAED pattern, typical for samples that contain nanoscale randomly oriented particles (Figure 7B,E,H). These Mn oxide sheets were often observed in association to calcite particles. Diffraction rings were observed at ~2.9, 2.5, 1.7, 1.5, 1.3, 1.1, and 1.0 Å, but it was not possible to determine what mineral phase this was based on these data. HRTEM images further showed that the ~2.5 Å interlayer distance broadened into the ~2.8 Å distance, similar distances as observed at lattice fringes in the type 1 area (Figure 7E). Type 3 areas, characterized by nanoscale particles on a plate-like material, were only rarely observed (Figure 7C). Individual particles had a diameter of approximately 3–6 nm. HRTEM images and the corresponding fast Fourier Transform (FFT) patterns show two main distances, 1.6–1.7 Å and 2.6–2.7 Å (Figure 7F,I).

EDS analyses indicated that the Mn:O atomic ratio varied considerably between the three identified type areas. The type 1 areas contained an unusually large amount of Mn, with a Mn:O atomic ratio of 1:0.6. The corresponding value for the denser type 2 areas was 1:1.3 and for the type 3 areas 1:2.1. Even though these ratios are based on qualitative measurements, they provide an indication of the relative difference between these areas. Considering that the expected atomic ratio for Mn dioxides (MnO_2) is 1:2, these results suggest that the thin elongated sheets in type 1 areas contain a larger amount of Mn(II/III) than do the other areas, possibly both incorporated into the mineral structure and adsorbed to mineral surfaces or associated with organic material. These findings are in agreement with total elemental analyses which indicated that, in addition to Mn (III) and Mn (IV), Mn(II) was present in significant amounts in the field site precipitate in Ytterby [15]. Since dissolved Mn(II) acts as a reducing agent for higher Mn oxides, the amount of Mn(II) in a system has a substantial influence on the solubility and stability of the precipitated phases [6]. In a recent paper, Jung et al. (2020) [42] showed that transformation of birnessite-type Mn oxides to tunnel structures such as todorokite was related to repeated redox cycles between Mn(II) and Mn(IV).

4.4. Manganese Phases and Oxidation States in the Samples Based on XANES Analyses

Manganese K-edge XANES data indicated that Mn binding environment and average oxidation state (reflecting the relative proportions of Mn(II), Mn(III), and Mn(IV) species) varied among the isolated species and the field samples (denoted YBS_1, YBS_2, and YBS_3) (Figure 8). The XANES spectra of precipitates formed in the *Cladosporium* co-culture and the mixed *Nevskia-Rhizobium* spp. cultures showed strong resemblance to that of Mn(II) bound to humic acid (both absorption edge position and post-edge features), suggesting a dominance of Mn(II) species sorbed on organics (e.g., biomass or/and bacterial cells) in these precipitates. However, the 1st derivatives of the XANES spectra of these

precipitates displayed a shoulder at approximately 6551 eV, where small peaks were also observed in the XANES derivatives of several Mn(III) oxide references (Figure 8B). The presence of the shoulder might suggest that low amounts of Mn(III) oxides also occur in these precipitates. In contrast, the absorption maxima for the spectra of *Hydrogenophaga* sp. and the three field site samples (i.e., YBS_1, YBS_2, and YBS_3) shifted to higher energies and matched with those of the birnessite (phyllomanganates) and todorokite (tectomanganates) references. Also, the pre-edge region of these spectra displayed a double-hump centering at 6541–6543 eV, a feature frequently reported for both birnessite and todorokite in octahedral coordination [30]. These features collectively suggest that Mn in the *Hydrogenophaga* sp. sample and all YBS samples occurs predominantly as birnessite- or todorokite-like phases, which can trap various amounts of Mn(IV) and Mn(III) in lattice positions, as well as surface-sorbed Mn(III)/Mn(II) species [63,64]. In addition, the XANES spectra and the 1st derivatives of the YBS samples also displayed two distinct features that are absent in the spectra of the birnessite and todorokite references: a broad shoulder and sub-peak centering approximately 6553 and 6548 eV, respectively. Since the XANES spectrum of Mn(II) sorbed on humic acid and its derivative displayed strong peaks at these energies, the presence of these two additional features might reflect considerable contributions of organically complexed Mn(II) in the YBS samples, in particular YBS_3.

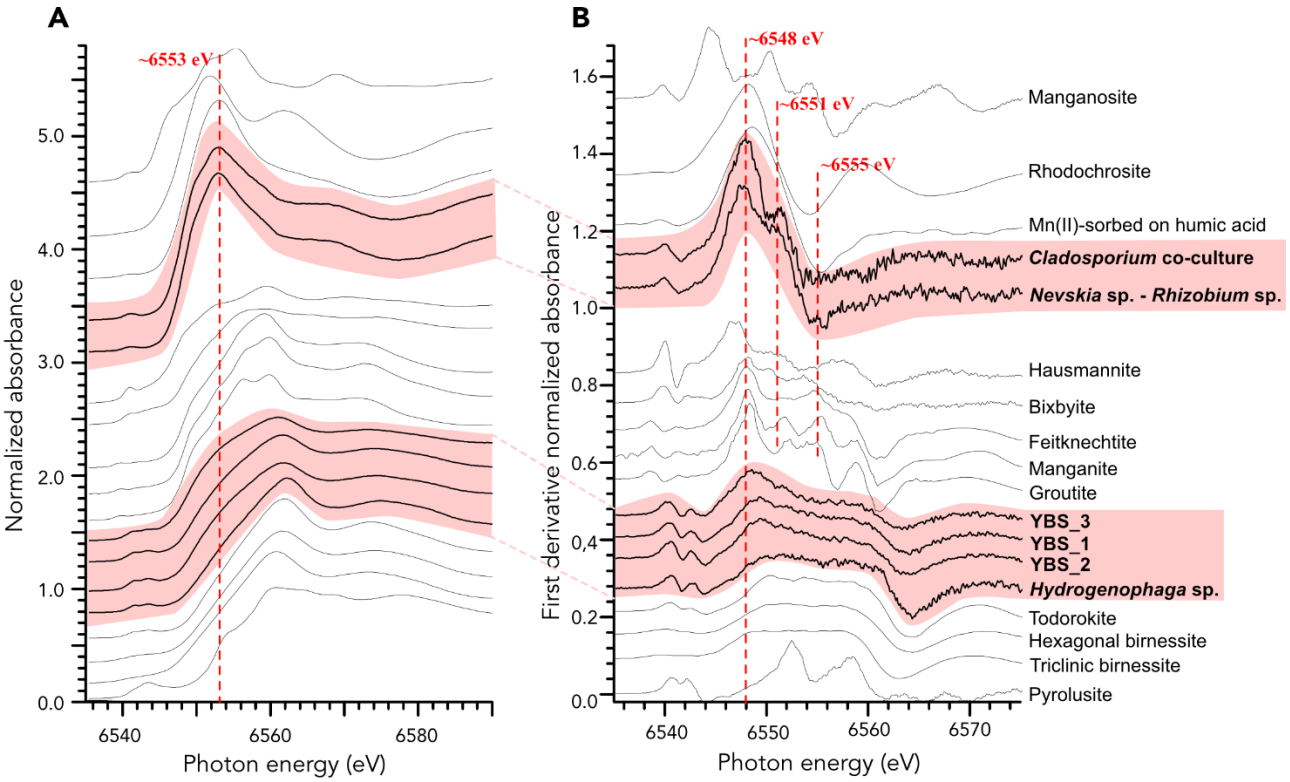

Figure 8. Mn K-edge XANES spectra. (**A**) Samples and reference compounds. (**B**) First derivatives of (**A**). The spectra of feitknechtite (β-MnOOH), manganite (γ-MnOOH), and groutite (α-MnOOH) were taken from Bargar et al. (2005) [6], while those of todorokite, rhodochrosite, and two hydrous layered phyllomanganates (hexagonal birnessite and triclinic birnessite) from Feng et al. (2010) [30] and Yu et al. (2017) [31], respectively.

Average oxidation state (AOS) of Mn in each sample was calculated using a calibration curve established based on a linear correlation between Mn oxidation state and pre-edge centroid energies of selected references. These reference compounds and the measured samples shared similar Mn coordination environment in their first shell (Figure 9A; detailed information is given in S4: Average Mn valence based on pre-edge peaks). The average bulk Mn oxidation state in YBS_1, YBS_2, and YBS_3 was estimated to 3.43, 3.51,

and 3.37, respectively. These values support a relatively high proportion of Mn(II) and possibly also Mn(III)-containing phases, in particular in YBS_3. An average oxidation state of 3.44 or higher was previously estimated from elemental analysis of what was defined as a birnessite phase, based on XRD-analysis [15]. The estimated AOS for Mn in *Nevskia-Rhizobium* spp. (2.56) and *Cladosporium* sp. co-culture (2.49) cultures (calculated from multiple merged scans recorded at the same spot) are in agreement with a strong affinity with Mn(II) bound to humic acid combined with low amounts of Mn(III) phases. However, TEM data associated to both species show that there are likely more than one mineral phase present in the samples. It is thus possible that the XANES data only represents one of these phases. The *Hydrogenophaga* sp. cultures showed the highest average Mn oxidation state (3.67), in agreement with the strong similarity between the XANES spectra of this sample and the todorokite/birnessite references.

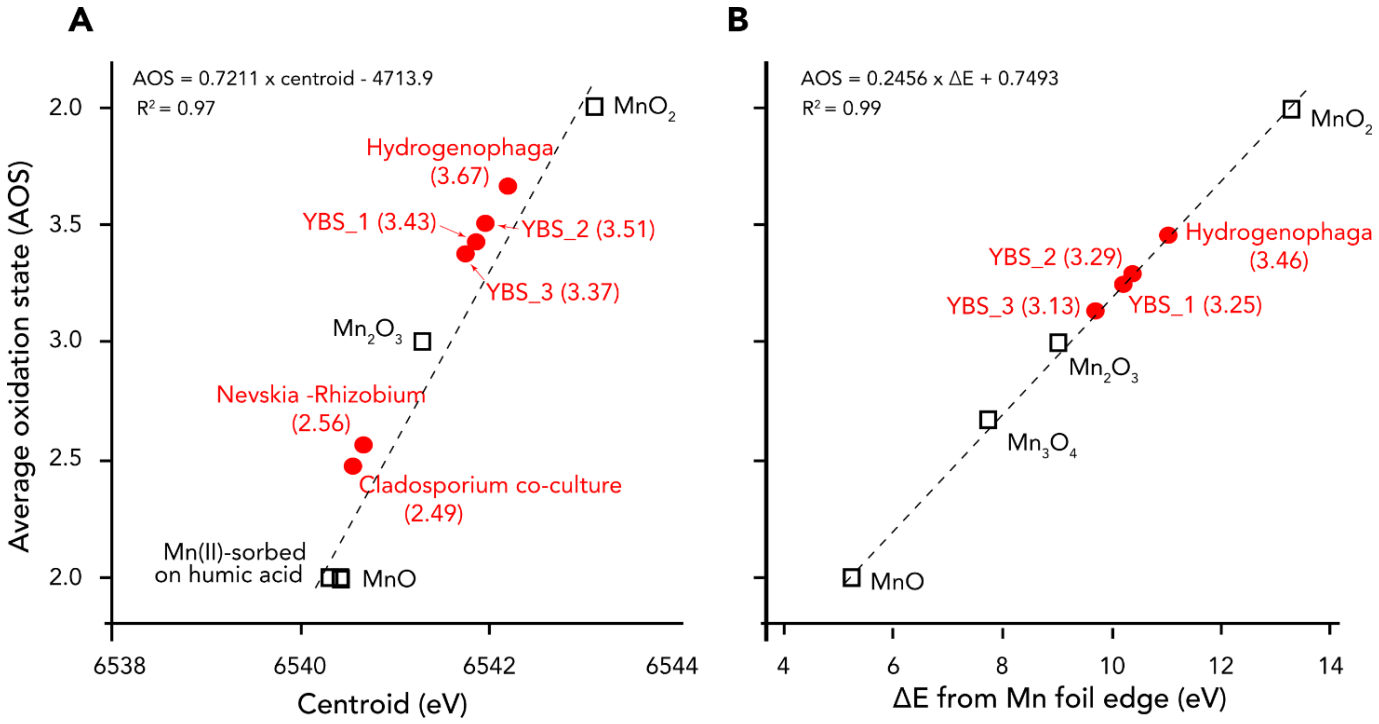

Figure 9. (**A**) Estimation of average oxidation state (AOS) of Mn in samples, using a calibration curve established based on a linear correlation between Mn oxidation state and pre-edge centroid energies of selected reference compounds with similar Mn coordination environment in the first shell as the samples (detailed information are given in S4). (**B**) For the samples with a dominance of MnO_x, AOS of Mn was also estimated based on the energy shifts on the absorption edge relative to Mn foil (ΔE) of known Mn oxidation states. The estimated AOS of Mn for each sample is also indicated in parentheses.

The AOS of Mn in MnO_x samples was cross-checked with another approach using the absorption edge energy relative to the Mn Foil, (ΔE)-methodology, which can be more sensitive to well-oxidized mineral phases (MnO_x samples). The values of AOS estimated by this approach were consistently 0.20 units lower than the values calculated with the pre-edge centroid approach (Figure 9). This indicates that the contributions of Mn(II) and possibly Mn(III) in the MnO_x samples may be even larger than assessed with the latter approach as presented above.

4.5. Promotion of Mn Oxidation by Biofilm Formation

Bacteria forming biofilms were more likely to precipitate Mn oxides in the culturing experiments than colonies growing in liquid media. This is exemplified by *Pedobacter* sp., which oxidized and precipitated Mn grown on solid substrates, but showed no capability of Mn oxidation as free floating cells in liquid media. The promotion of Mn oxidation by biofilm formation was previously documented by Nealson and Ford (1980) [65], who observed that a *Bacillus* species had little or no Mn-oxidizing capability as a free floating cell, but showed a drastic increase in Mn oxidation rate once the bacterium interacted with solid substrates. Deposition of Mn oxides in the Ytterby mine tunnel is also associated with a group of bacteria forming epilithic biofilms [8,32]. This type of biofilm is beneficial for Mn oxidation partly due to the potential as nucleation site for Mn mineralization, but also for the capacity of binding elements to acidic groups within the biofilm, thus acting as storage for further use or for neutralization purposes.

Mn(II) ions are attracted by the negatively charged carboxyl and phosphoryl groups on the bacterial cell wall or in the extracellular secretions. Sorbed Mn(II) is then oxidized to Mn(III/IV) either enzymatically (direct), using molecular oxygen and/or hydrogen peroxide (H_2O_2) as substrates, or indirect, as a response to metabolically produced reactive oxygen species (ROS) known to be produced in larger quantities during the exponential growth phase [66]. Oxidized Mn then precipitates within or in association to the biofilm. Catalysis of Mn(II) oxidation by already formed Mn oxides, i.e., autocatalytical oxidation through the reduction of MnO_2, is also expected when the initial product is formed [1,6]. MnO_2 is one of the strongest oxidants in nature.

4.6. Sequestration of Mn Oxides in the Ytterby Mine Tunnel—A Proposed Model of Formation

Figure 10, summarizes the biologically mediated Mn oxidation and precipitation process in the Ytterby mine tunnel. This mechanistic description of the studied system is fed by data from the field site and culture work, summarizing information about the involved microbial population, interpreted associated metabolic processes, both organic and mineral products, within a well physicochemically constrained environment. Data from the present study are integrated with previously published results on the spatial distribution of elements and microorganisms as well as environmental parameters in this ecosystem [8,15,32,67].

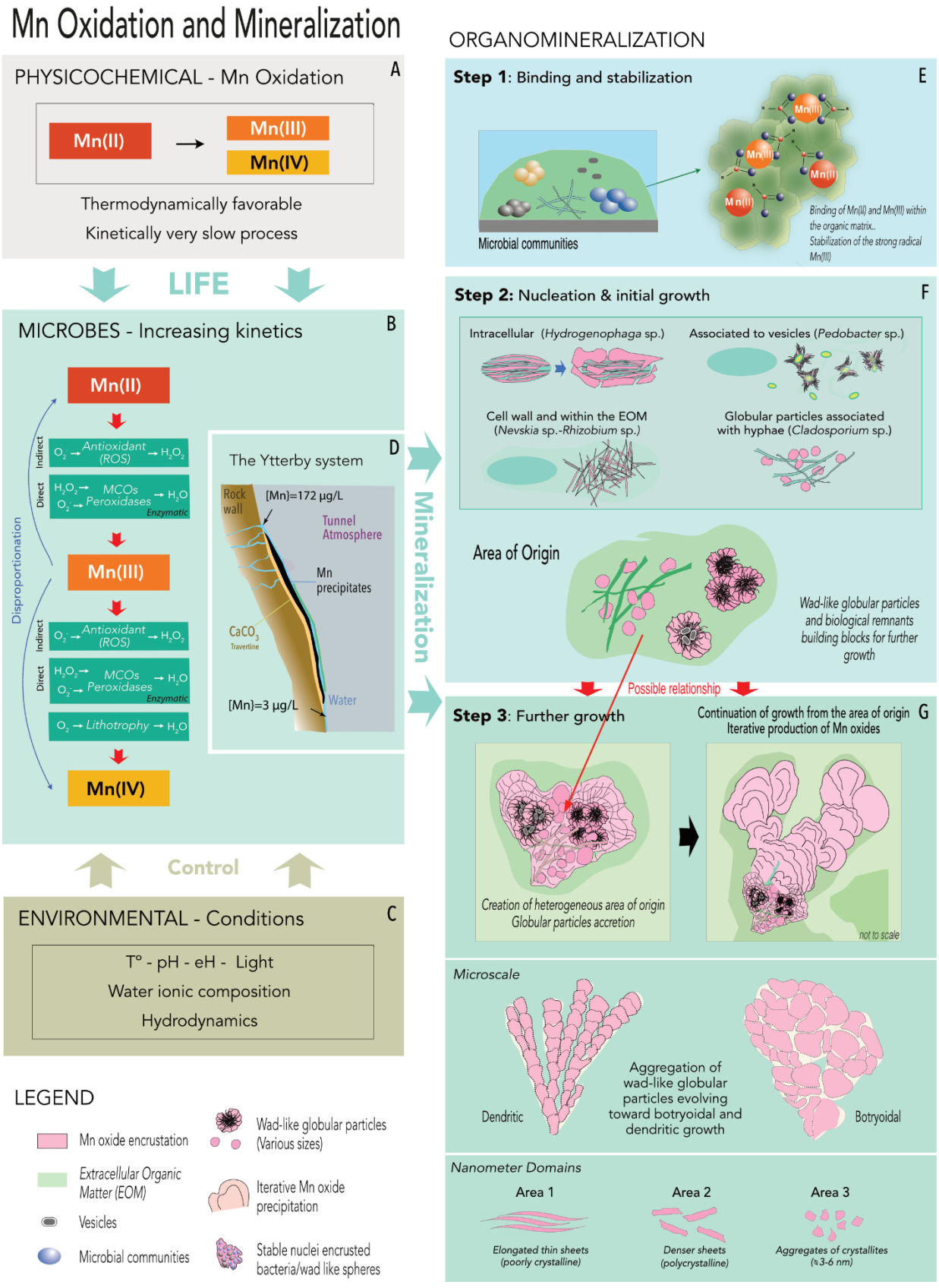

Figure 10. Sequestration of Mn oxides in the Ytterby mine tunnel—a proposed model of formation. This model provides a general view of the system showing the development of the Mn oxide producing biofilm and associated mineralizations. See Section 4.6 for a detailed description.

In the Ytterby mine system (Figure 10D), water seeping from the bedrock fracture contains aqueous Mn (172 μg/L) and REE (11 μg/L), but very low amounts of Fe (0.4 μg/L) and host communities with high phylogenetic diversity and species richness [8]. Water percolates across the rock surface. Planktonic populations settle to produce a thin biofilm at the rock surface. Mn(II/III) and REE are progressively bound to the organic matter in the biofilm (cells and extracellular organic matter; EOM). The Mn concentration in the water drops drastically from 172 μg/L when the water emerges from the fracture to 3 μg/L after it has passed through the Mn precipitates down the 2 m tall rock wall [8]. This strong attenuation of aqueous Mn is coupled to enrichment of insoluble Mn oxides in the biofilm, which in turn attracts other metals, notably REE. With the help of the stabilizing action of organic ligands (i.e., biofilm formation), the epilithic microbial communities induce the two-step oxidation (Mn(II) to Mn(III) and Mn(III) to Mn(IV), through direct and indirect processes, leading to the final formation of mainly birnessite-type Mn oxides (Figure 10B).

This mineralization process includes three main steps: (1) binding and stabilization of aqueous Mn by organic ligands (Figure 10E), (2) nucleation and initial growth (Figure 10F), and (3) further growth (Figure 10G).

Step 1 (Figure 10E): Prokaryotic communities that are adapted to the mine environment (no light, low temperature) thrive and become enriched within the biofilm, over time creating an environment rich in metals [8]. The negatively charged Mn oxides sorb additional Mn(II) as well as trace metals. The high binding efficiency of the combined organic and mineral substrates constitutes a powerful sponge for positively charged ions, exemplified by the steep drop in Mn(II) concentration between the top and bottom water. The gradual sequestration of metals leads to the extreme nature of the YBS biofilm.

Step 2 (Figure 10F): Culture-based data suggest that initial nucleation and growth in a biofilm is dependent on community-specific strategies for utilizing aqueous Mn and its solid phases. Bacteria such as the *Hydrogenophaga* sp. precipitate Mn within the cell, leading to their demise (Figure 2). Other bacteria develop strategies for oxidizing and sequestrating Mn away from the cell. This is exemplified by the *Pedobacter* strain, which seems to use vesicles, transported from the cell membrane out to the extracellular organic matrix, as the preferred location for Mn precipitation (Figure 3F–H), or the *Nevskia-Rhizobium* spp., which are observed with mineralized stalks and extracellular organic matter (Figure 4E,F). Also, the *Cladosporium* sp. co-culture primarily deposit globular Mn particles spatially separated from the hyphae (Figure 5). These depositional strategies seem to be associated with different mineral products. As indicated by XANES and TEM data, Mn oxides occur as a range of structurally diverse phases incorporating Mn of various oxidation states (Figures 4, 7–9 and S3). A common trait in the observed minerals is that nucleation and initial growth are closely related to the microbial community and biofilm formation. This interaction between organics and minerals leads to the formation of an area of origin from which the future Mn oxide mineral will grow and develop. The areas of origin are highly heterogeneous in terms of mineral phases, incorporation of organic matter, as well as oxidation state of the incorporated Mn. It is likely that highly reactive Mn(III) produced by the first oxidation step can be stabilized within the EOM and the Mn minerals.

Step 3 (Figure 10G): Further growth: In both the field site samples and samples retrieved from associated cultures, the precipitation of Mn oxides is initiated in areas strongly influenced by microbes (Figure 6A,B). However, a knowledge gap exists between the formation of this area of origin and further growth into more developed Mn oxide crystals as no such mineral development was observed in cultures. In field site samples, further growth from the initial mineralization area mainly seem to occur by incorporation or aggregation of specific building blocks observed as wad-like globular particles (Figure 6D–H). These wad-like globular Mn oxide particles either form the base for further growth into dendrites-botryoids or fuse onto an existing structure. In the field site samples, there are at least three nanoscale type areas: with long fiber, denser sheets, and aggregates of more stocky crystallites (see also Figure 7). Microbial traces encrusted by Mn oxides are primarily associated with the initial growth areas (area of origin). The relatively chaotic

mix of organic traces and early Mn oxide particles serves as a stable nucleus for further growth. This initial growth area becomes capped by denser, laminated precipitates, which implies an iterative growth process.

5. Conclusions

Cultures based on samples from the Mn rock wall deposit in the Ytterby mine yielded four bacterial (*Hydrogenophaga* sp., *Pedobacter* sp., *Rhizobium* sp., and *Nevskia* sp.) strains and one fungal-bacterial co-culture (*Cladosporium* sp.—*Hydrogenophaga* sp. *Rhizobium* sp.—*Nevskia* sp.), with varying abilities to deposit minerals containing oxidized Mn. Pure cultures were obtained of the *Hydrogenophaga* sp. as well as the *Pedobacter* sp., while the *Rhizobium* sp. and *Nevskia* sp. only precipitated Mn oxides when growing together. As for the *Cladosporium* sp. co-cultures, the bacterial species were not detected in microscopy images, but were present in the rRNA gene sequence analysis. We assume, that these cultures were dominated by *Cladosporium* sp., but that the bacterial consortium was present in varying proportions.

Culturing experiments show that taxonomic affiliation influence crystallite size, structure, and average Mn oxidation state as well as the onset location of Mn precipitation with respect to the cells. *Hydrogenophaga* sp. accumulate Mn oxide precipitates in a well constrained area in the center of the colonies. Early mineral deposition is mediated by the cells, but non-biological processes appear to be responsible at later stage processes. The *Pedobacter* strain produces large amounts of a slimy mucilaginous mass in which abundant spherical Mn oxides form, possibly in association with double-layer membrane vesicles released from the cells. Mixed *Nevskia-Rhizobium* spp. cultures produce long colony strings with a dark hazy center and entire to undulating margins in which Mn precipitates are located. Mn precipitates are deposited on *Nevskia* sp. cell surfaces and on what is assumed to be acellular stalks. *Rhizobium* sp. has electron dense intracellular areas that mainly contain NaCl, but also small amounts of Mn. The retrieved Mn-oxidizing fungal-bacterial co-culture primarily deposit Mn oxide globular particles that are spatially separated from the hyphae, but also knot-like aggregates deposited on hyphal surfaces. With time, large aggregates of Mn oxides form in all studied bacterial colonies. Crystal growth occurs at the outer edges of these larger well-developed crystals.

Results also show that growth conditions (biofilm or planktonic) could prove decisive for the ability to oxidize Mn and precipitate minerals containing oxidized Mn.

The onset of Mn oxide mineralization at the field site is more difficult to interpret, but typically occurs in areas associated with globular wad-like particles and microbial traces. The wad-like particles serve as building blocks in the majority of the microstructures, either forming the base for further growth into dendrites-botryoids or added as components to an existing structure. The relatively chaotic mix of organic traces and early Mn oxide particles become capped by laminated precipitates, implying an iterative growth process. The most commonly observed nanoscale structure is networks of Mn oxide sheets that are structurally related to birnessite. Data suggest that these thin elongated sheets contain an unusually large amount of Mn with respect to oxygen. In agreement with previous total analyses of field site samples [15], results on atomic absorption indicate that, in addition to Mn (III) and Mn (IV), Mn(II) is present in significant amounts. XANES results suggest that the average Mn oxidation state in the field site precipitates (YBS) is 3.4–3.5, in agreement with previous estimates.

Supplementary Materials: The following are available online at www.mdpi.com/article/10.3390/min11101146/s1, Figure S1: QIIME2 workflow for Microbe-mediated Mn-oxidation, Figure S2: Sequence reads, Figure S3: *Hydrogenophaga* sp. and associated Mn precipitates, Figure S4: Quantification of average Mn valence based on pre-edge peaks.

Author Contributions: Conceptualization, S.S. and C.D.; Data curation, S.S., C.Y., C.W.S., S.H., M.Å. and C.D.; Formal analysis, S.S., C.Y., C.W.S., R.H., B.A., M.Å. and C.D.; Funding acquisition, C.D., S.S., C.W.S. and S.H.; Methodology, S.S., C.Y., C.W.S., R.H., S.H., M.Å. and C.D.; Visualization, S.S.,

C.Y., S.H. and C.D.; Writing—original draft, S.S., C.D. and C.Y.; Writing—review & editing, S.S., C.Y., C.W.S., B.A., R.H., S.H., M.Å. and C.D. All authors have read and agreed to the published version of the manuscript.

Funding: This research was funded by Swedish Research Council grant number 2018-04167_VR awarded to CD, Faculty of Science at Stockholm University, SciLifeLab grant number SU FV-2.1.1-1843-17 awarded to CD and SS, Swedish Research Council grant number VR-FRI 2019-00217 awarded to Umeå Center for Electron Microscopy (UCEM) at Umeå University and the National Microscopy Infrastructure and Swedish Researh Council] grant number 2020-05071 awarded CWS. We acknowledge MAX IV Laboratory for time on Balder Beamline under Proposal 20190277. Research conducted at MAX IV, a Swedish national user facility, is supported by the Swedish Research council under contract 2018-07152, the Swedish Governmental Agency for Innovation Systems under contract 2018-04969, and Formas under contract 2019-02496. The APC was funded by Stockholm University Library.

Acknowledgments: The authors would like to thank the Swedish Fortifications Authority for allowing access to the Ytterby mine and for sharing data on this locality. Access to laboratory facilities as well as assistance at the Ettema Lab, Biomedical Center (BMC) at Uppsala University is gratefully acknowledged. Assistance in sample preparation and microscopy at the Umeå Center for Electron Microscopy (UCEM) at Umeå University and the National Microscopy Infrastructure, NMI, is gratefully acknowledged with a special thanks to Cheng Choo Lee. Many thanks to Anumol Ashok and-Kjell Jansson at the Department of Materials and Environmental Chemistry, Stockholm University for providing technical assistance to conduct SEM and TEM. The MAX IV Laboratory is acknowledged for time on the Balder Beamline under Proposal 20190277.

Conflicts of interest: The authors declare no conflicts of interest.

References

1. Tebo, B.M.; Bargar, J.R.; Clement, B.G.; Dick, G.J.; Murray, K.J.; Parker, D.; Verity, R.; Webb, S.M. Biogenic manganese oxides: Properties and mechanisms of formation. *Annu. Rev. Earth Planet. Sci.* **2004**, *32*, 287–328.
2. Luther, G.W., III. The role of one- and two-electron transfer reactions in forming thermodynamically unstable intermediates as barriers in multi-electron redox reactions. *Aquat. Geochem.* **2010**, *16*, 395–420.
3. Morgan, J.J. Kinetics of reaction of O_2 and Mn(II) species in aqueous solutions. *Geochim. Cosmochim. Acta* **2005**, *69*, 35–48.
4. Hansel, C.M.; Learman, D.R. Geomicrobiology of manganese. In *Ehrlich's Geomicrobiology*, 6th ed.; Ehrlich, H.L., Newman, D.K., Kappler, A., Eds.; CRC Press: Boca Raton, FL, USA, 2016; pp. 401–452.
5. Zhou, D.; Kim, D.-G.; Ko, S.-O. Heavy metal adsorption with biogenic manganese oxides generated by *Pseudomonas putida* strain MnB1. *J. Ind. Eng. Chem.* **2015**, *24*, 132–139.
6. Bargar, J.R.; Tebo, B.M.; Bergmann, U.; Webb, S.M.; Glatzel, P.; Chiu, V.Q.; Villalobos, M. Biotic and abiotic products of Mn(II) oxidation by spores of the marine *Bacillus* sp. strain SG-1. *Am. Mineral.* **2005**, *90*, 143–154.
7. Webb, S.M.; Tebo, B.M.; Bargar, J.R. Structural influences of sodium and calcium ions on the biogenic manganese oxides produced by the marine Bacillus sp., strain SG-1. *Geomicrobiol. J.* **2005**, *22*, 181–193.
8. Sjöberg, S.; Stairs, C.W.; Allard, B.; Homa, F.; Martin, T.; Sjöberg, V.; Ettema, T.J.; Dupraz, C. Microbiomes in a manganese oxide producing ecosystem in the Ytterby mine, Sweden: Impact on metal mobility. *FEMS Microbiol. Ecol.* **2020**, *96*, 11.
9. Sun, W.; Kitchaev, D.A.; Kramer, D.; Ceder, G. Non-equilibrium crystallization pathways of manganese oxides in aqueous solution. *Nat. Commun.* **2019**, *10*, 573.
10. Enghag, P. Jordens Grundämnen Och Deras Upptäckt, Sällsynt-Ädelt-Aktivt. Industrilitteratur AB: Stockholm, Sweden, 1999.
11. Nordenskjöld, I. *Ytterby Fältspatbrott. Skandinavisk Tidskrift för Lervaru- och Stenindustri. Organ för Tegel, Cement, Beton, Kalk, Sten Och Byggnadsmaterialier*; N:o 6 &7; Stockholm, Sweden, 1904. (In Swedish)
12. Sjöberg, S. The Ytterby Mine—A Historical Review and an Evaluation of Its Suggested Spatial Coupling to Multiple Sclerosis (MS). Bachelor's Thesis. Stockholm University, Stockholm, Sweden, 2012.
13. Sjöberg, S. Characterization of an REE-Enriched Black Substance in Fractured Bedrock in the Ytterby Mine. Master's Thesis. Stockholm University, Stockholm, Sweden, 2014.
14. Cailleau, G.; Verrecchia, E.P.; Braissant, O.; Emmanuel, L. The biogenic origin of needle fibre calcite. *Sedimentology* **2009**, *56*, 1858–1875.
15. Sjöberg, S.; Allard, B.; Rattray, J.E.; Callac, N.; Grawunder, A.; Ivarsson, M.; Sjöberg, V.; Karlsson, S.; Skelton, A.; Dupraz, C. Rare earth element enriched birnessite in water-bearing fractures, the Ytterby mine, Sweden. *Appl. Geochem.* **2017**, *78*, 158–171.
16. Swedish Fortifications Agency (Fortifikationsverket). *Utredningsprogram Ytterby, Vaxholms Kommun*; 4:610, 4:564, 4:611. 4:9, Rev, A; Swedish Fortifications Agency: Eskilstuna, Sweden, 2012.
17. Krumbein, W.E.; Altmann, H.J. A new method for the detection and enumeration of manganese oxidizing and reducing microorganisms. *Helgoländer Wiss. Meeresunters.* **1973**, *25*, 347–356.

18. Tebo, B.M.; Clement, B.G.; Dick, G.D. Biotransformations of manganese. In *Manual of Environmental Microbiology*, 3rd ed.; Hurst, C.H., Ed.; ASM Press: Washington, DC, USA, 2007; pp. 1223–1238.
19. Spang, A.; Saw, J.H.; Jørgensen, S.L.; Zaremba-Niedzwiedzka, K.; Martijn, J.; Lind, A.E.; van Eijk, R.; Schleper, C.; Guy, L.; Ettema, T.J.G. Complex archaea that bridge the gap between prokaryotes and eukaryotes. *Nature* 2015, 521, 173–179.
20. Bolyen, E.; Rideout, J.R.; Dillon, M.R.; Bokulich, N.A.; Abnet, C.C.; Al-Ghalith, G.A.; Alexander, H.; Alm, E.J.; Arumugam, M.; Asnicar, F.; et al. Reproducible, interactive, scalable and extensible microbiome data science using QIIME2. *Nat. Biotechnol.* **2019**, *37*, 852–857.
21. Bokulich, N.; Robeson, M.; Dillon, M.; Ziemski, M.; Kaehler, B.; O'Rourke, D. *Bokulich-Lab/RESCRIPt: 2021.8.0.dev0 (Zenodo, 2021)*; 2021. Available online: https://zenodo.org/record/4811136#.YWlYdRpByUk (accessed on 20 August 2021).
22. Pruesse, E.; Quast, C.; Knittel, K.; Fuchs, B.M.; Ludwig, W.; Peplies, J.; Glöckner, F.O. SILVA: A comprehensive online resource for quality checked and aligned ribosomal RNA sequence data compatible with ARB. *Nucleic Acids Res.* **2007**, *35*, 7188–7196.
23. NCBI Sequence Read Archive (SRA). Available online: https://www.ncbi.nlm.nih.gov/sra (accessed on 20 August 2021).
24. Dupraz, C.; Fowler, A.; Tobias, C.; Visscher, P.T. Stromatolic knobs in Storr's lake (San Salvador, Bahamas): A model system for formation and alternation of laminae. *Geobiology* **2013**, *11*, 527–548.
25. Hawes, P.; Netherton, C.L.; Mueller, M.; Wileman, T.; Monaghan, P. Rapid freeze- substitution preserves membranes in high pressure frozen tissue culture cells. *J. Microsc.* **2007**, *226*, 182–189.
26. Reynolds, E.S. The use of lead citrate at high pH as an electron-opaque stain in electron microscopy. *J. Cell Biol*. **1963**, *17*, 208–212.
27. Klementiev, K.; Norén, K.; Carlson, S.; Clauss Sigridsson, K.; Persson, I. The BALDER Beamline at the MAX IV Laboratory. *J. Phys. Conf. Ser*. **2016**, *712*, 01223.
28. Yu, C.X.; Virtasalo, J.J.; Österholm, P.; Burton, E.D.; Peltola, P.; Ojala, A.E.K.; Hogmalm, J.K.; Åström, M.E. Manganese accumulation and solid-phase speciation in a 3.5 m thick mud sequence from the estuary of an acidic and Mn-rich creek, northern Baltic Sea. *Chem. Geol.* **2016**, *437*, 56–66.
29. Ravel, B.; Newville, M. ATHENA, ARTEMIS, HEPHAESTUS: Data analysis for X-ray absorption spectroscopy using IFEFFIT. *J. Synchrotron Radiat.* **2005**, *12*, 537–541.
30. Feng, X.H.; Zhu, M.; Ginder-Vogel, M.; Ni, C.; Parikh, S.J.; Sparks, D.L. Formation of nano-crystalline todorokite from biogenic Mn oxides. *Geochim. Cosmochim. Acta* **2010**, *74*, 3232–3245.
31. Yu, C.; Drake, H.; Mathurin, F.A.; Åström, M.E. Cerium sequestration and accumulation in fractured crystalline bedrock: The role of Mn-Fe (hydr-)oxides and clay minerals. *Geochim. Et Cosmochim. Acta* **2017**, *199*, 370–389.
32. Sjöberg, S.; Stairs, C.; Allard, B.; Hallberg, R.; Homa, F.; Martin, T.; Ettema, T.J.G.; Dupraz, C. Bubble biofilm: Bacterial colonization of air-air interface. *Biofilm* **2020**, *2*, 100030.
33. Marcus, D.N.; Pinto, A.; Anantharaman, K.; Ruberg, S.A.; Kramer, E.L.; Raskin, L.; Dick, G.J. Diverse manganese(II)-oxidizing bacteria are prevalent in drinking water systems. *Environ. Microbiol. Rep.* **2017**, *9*, 120–128.
34. Dangeti, S.; McBeth, J.M.; Roshani, B.; Vyskocil, J.M.; Rindall, B.; Chang, W. Microbial communities and biogenic Mn-oxides in an on-site biofiltration system for cold Fe-(II)- and Mn(II)-rich groundwater treatment. *Sci. Total Environ.* **2020**, *710*, 136386.
35. Bohu, T.; Akob, D.M.; Abratis, M.; Lazar, C.S.; Küsel, K. Biological low-pH Mn(II) oxidation in a manganese deposit influenced by metal-rich groundwater. *Appl. Environ. Microbiol.* **2016**, *82*, 3009–3021.
36. Mota, E.A.; Felestrino, E.B.; Leão, V.A.; Guerra-Sá, R. Manganese (II) removal from aqueous solution by *Cladosporium Halotolerans* and *Hypocrea jecorina. Biotechn. Rep*. **2020**, *25*, e00431.
37. Shao, Z.; Sun, F. Intracellular sequestration of manganese and phosphorous in a metal-resistant fungus Cladosporium cladosporioides from deep-sea sediment. *Extremophiles*. **2007**, *11*, 435–443.
38. Drits, V.A.; Silvester, E.; Gorshkov, A.I.; Manceau, A. Structure of synthetic monoclinic Na-rich birnessite and hexagonal birnessite: I. Results from X-ray diffraction and selected-area electron diffraction. *Am. Mineral*. **1997**, *82*, 946–961.
39. Villalobos, M.; Toner, B.; Bargar, J.; Sposito, G. Characterization of the manganese oxide produced by *Pseudomonas putida* strain MnB1. *Geochim. Cosmochim. Acta* **2003**, *67*, 2649–2662.
40. Villalobos, M.; Lanson, B.; Manceau, A.; Toner, B.; Sposito, G. Structural model for the biogenic Mn oxide produced by *Pseudomonas putida*. *Am. Mineral.* **2006**, *91*, 489–502.
41. Atkins, A.L.; Shaw, S.; Peacock, C.L. Nucleation and growth of todorokite from birnessite: Implications for trace-metal cycling in marine sediments. *Geochim. Cosmochim. Acta* **2014**, *144*, 109–125.
42. Jung, H.; Taillefert, M.; Sun, J.; Wang, Q.; Borkiewicz, O.J.; Liu, P.; Yang, L.; Chen, S.; Chen, H.; Tang, Y. Redox cycling driven transformation of layered manganese oxides to tunnel structures. *J. Am. Chem. Soc*. **2020**, *142*, 2506–2513.
43. Gabr, R.M.; Hassan, S.H.A.; Shoreit, A.A.M. Biosorption of lead and nickel by living and non-living cells of *Pseudomonas aeruginosa* ASU 6a. *Int. Biodeterior. Biodegrad*. **2008**, *62*, 195–203.
44. Larsen, E.I.; Sly, L.I.; McEwan, A.G. Manganese(II) adsorption and oxidation by whole cells and a membrane fraction of *Pedomicrobium* sp. ACM 3067. *Arch. Microbiol.* **1999**, *171*, 257–264.
45. Ghiorse, W.C.; Hirsch, P. An ultrastructural study of iron and manganese deposition associated with extracellular polymers of *Pedomicrobium*-like budding bacteria. *Arch. Microbiol.* **1979**, *123*, 213–226.
46. De Vrind, J.; de Groot, A.; Brouwers, G.J.; Tommassen, J.; de Vrind–de Jong, E. Identification of a novel Gsp-related pathway required for secretion of the manganese-oxidizing factor of *Pseudomonas putida* strain GB-1. *Mol. Microbiol.* **2003**, *47*, 993–1006.

47. Emerson, D.; Ghiorse, W.C. Ultrastructure and chemical composition of the sheath of *Lepthothrix discophora* SP-6. *J. Bacteriol.* **1993**, *175*, 7808–7818.
48. Okazaki, M.; Sugita, T.; Shimizu, M.; Ohode, Y.; Iwamoto, K.; de Vrind de Jong, E.W.; de Vrind, J.P.M.; Corstjens, P.L.A.M. Partial purification and characteriazation of manganese oxidizing factors of *Pseudomonas fluorescens* GB-1. *Appl. Environ. Microbiol.* **1997**, *63*, 4793–4799.
49. Francis, C.A.; Tebo, B.M. Marine *Bacillus* spores as catalysts for oxidative precipitation and sorption of metals. *J. Molec. Microbiol. Biotechnol.* **1999**, *1*, 71–78.
50. Francis, C.A.; Casciotti, K.L.; Tebo, B.M. Localization of Mn(II)-oxidizing activity and the putative multicopper oxidase, MnxG, to the exosporium of the marine *Bacillus* sp. strain SG-1. *Arch. Microbiol.* **2002**, *178*, 450–456.
51. Nealson, K.H.; Tebo, B. Structural features of manganese precipitating bacteria. *Orig. Life Evol. Biosph.* **1980**, *10*, 117–126.
52. Daye, M.; Klepac-Ceraj, V.; Pajusalu, M.; Rowland, S.; Farrell-Sherman, A.; Beukes, N.; Tamura, N.; Fournier, G.; Bosak, T. Light-driven anaerobic microbial oxidation of manganese. *Nature* **2019**, *576*, 311–314.
53. Ehrlich, H.L.; Salerno, J.C. Energy coupling in Mn2+ oxidation by a marine bacterium. *Arch. Microbiol.* **1990**, *154*, 12–17.
54. Babenzien, H.D.; Cypionka, H.N. Nevskia. In *Bergey's Manual of Systematics of Archaea and Bacteria*; John Wiley & Sons Inc., in Association with Bergey's Manual Trust: Hoboken, NJ, USA, 2015; pp. 1–6.
55. Heldal, M.; Tumyr, O. Morphology and content of dry matter and some elements in cells and stalks of Nevskia from an eutrophic lake. *Can. J. Microbiol.* **1986**, *32*, 89–92.
56. Kim, S.J. New characterization of takanelite. *Am. Mineral.* **1991**, *76*, 1426–1430.
57. Post, J.E.; Heaney, P.J.; Ertl, A. Rietveld refinement of the ranciéite structure using synchrotron powder diffraction data. *Powder Diffr.* **2007**, *23*, 10–14.
58. Cygan, R.T.; Post, J.E.; Heaney, P.J.; Kubicki, J.D. Molecular models of birnessite and related hydrated layered minerals. *Am. Mineral.* **2012**, *97*, 1505–1514.
59. Grangeon, S.; Warmont, F.; Tournassat, C.; Lanson, B.; Lanson, M.; Elkaïm, E.; Claret, F. Nucleation and growth of feitknechtite from nanocrystalline vernadite precursor. *Eur. J. Mineral.* **2017**, *29*, 767–776.
60. Wegorzewski, A.V.; Kuhn, T.; Dohrmann, R.; Wirth, R.; Grangeon, S. Mineralogical characterization of individual growth structures of Mn-nodules with different Ni + Cu content from the central Pacific Ocean. *Am. Mineral.* **2015**, *100*, 2497–2508.
61. Chukrov, F.V. New mineral phases of oceanic manganese micronodules. *Int. Geol. Rev.* **1980**, *22*, 154–160.
62. Chukrov, F.V.; Drits, V.A.; Gorshkov, A.I.; Sakharov, B.A.; Dikov, Y.P. Structural models of vernadite. *Int. Geol. Rev.* **1987**, *29*, 1337–1347.
63. Learman, D.R.; Wankel, S.D.; Webb, S.M.; Martinez, N.; Madden, A.S.; Hansel, C.M. Coupled biotic-abiotic Mn (II) oxidation pathways mediates the formation and structural evolution of biogenic Mn oxides. *Geochim. Cosmochim. Acta* **2011**, *75*, 6048–6063.
64. Webb, S.M.; Tebo, B.M.; Bargar, J.R. Structural characterization of biogenic Mn oxides produced in seawater by the marine Bacillus sp. strain SG-1. *Am. Mineral.* **2005**, *90*, 1342–1357.
65. Nealson, K.H.; Ford, J. Surface enhancement of bacterial manganese oxidation: Implications for aquatic environments. *Geomicrobiol. J.* **1980**, *2*, 21–37.
66. Couasnon, T. Determination and Quantification of Reactive Oxygen Species (ROS) in Bacterial Biofilms. Rôle des Espèces Réactives de L'oxygène et Substance Exopolymériques des Bactéries Dans le Processus de Biominéralisation du Manganese. Ph.D. Thesis. Institute de Physique du Globe de Paris, Université Sorbonne Paris Cité, Paris, France, 2019; Chapter 3, pp. 51–88.
67. Sjöberg, S. Microbially Mediated Manganese Oxides Enriched in Yttrium and Rare Earth Elements in the Ytterby Mine. Ph. D. Thesis, Sweden. Stockholm University, Stockholm, Sweden, 2019.